Elsevier Editorial System(tm) for Geochimica et Cosmochimica Acta

Manuscript Draft

Manuscript Number: GCA-D-15-00159R2

Title: Target-projectile interaction during impact melting at Kamil Crater, Egypt

Article Type: Article

Corresponding Author: Dr. Agnese Fazio, Ph.D.

Corresponding Author's Institution: Friedrich-Schiller-Universität Jena

First Author: Agnese Fazio, Ph.D.

Order of Authors: Agnese Fazio, Ph.D.; Massimo D'Orazio; Carole Cordier; Luigi Folco

Abstract: In small meteorite impacts, the projectile may survive through fragmentation; in addition, it may melt, and chemically and physically interact with both shocked and melted target rocks. However, the mixing/mingling between projectile and target melts is a process still not completely understood. Kamil Crater (45 m in diameter; Egypt), generated by the hypervelocity impact of the Gebel Kamil Ni-rich ataxite on sandstone target, allows to study the target-projectile interaction in a simple and fresh geological setting. We conducted a petrographic and geochemical study of macroscopic impact melt lapilli and bombs ejected from the crater, which were collected during our geophysical campaign in February 2010. Two types of glasses constitute the impact melt lapilli and bombs: a white glass and a dark glass. The white glass is mostly made of SiO_2 and it is devoid of inclusions. Its negligible Ni and Co contents suggest derivation from the target rocks without interaction with the projectile (<0.1 wt% of projectile contamination). The dark glass is a silicate melt with variable contents of Al_2O_3 (0.84-18.7 wt%), FeOT (1.83-61.5 wt%), and NiO (<0.01-10.2 wt%). The dark glass typically includes fragments (from few μm to several mm in size) of shocked sandstone, diaplectic glass, lechatelierite, and Ni-Fe metal blebs. The metal blebs are enriched in Ni compared to the Gebel Kamil meteorite. The dark glass is thus a mixture of target and projectile melts (11-12 wt% of projectile contamination). Based on recently proposed models for target-projectile interaction and for impact glass formation, we suggest a scenario for the glass formation at Kamil. During the transition from the contact and compression stage and the excavation stage, projectile and target liquids formed at their interface and chemically interact in a restricted zone. Projectile contamination affected only a shallow portion of the target rocks. The SiO_2 melt that eventually solidified as white glass behaved as an immiscible liquid and did not interact with the projectile. During the excavation stage dark glass melt engulfed and coated the white glass melt, target fragments, and got stuck to iron meteorite shrapnel fragments. This model could also explain the common formation of white and dark glasses in small impact craters generated by iron bodies (e.g., Wabar).

Target-projectile interaction during impact melting at Kamil Crater, Egypt

Agnese FAZIO[1,2*], Massimo D'ORAZIO[1], Carole CORDIER[3,4], and Luigi FOLCO[1]

[1]Dipartimento di Scienze della Terra, Università di Pisa, Via S. Maria 53, I-56126 Pisa, Italy

[2] Present address: Analytische Mineralogie der Mikro- und Nanostrukturen, Institut für Geowissenschaften, Friedrich-Schiller-Universität Jena, Carl-Zeiss-Promenade 10, D-07745 Jena, Germany

[3]Université de Grenoble Alpes, ISTerre, BP 53, F-38041 Grenoble CEDEX 9, France

[4]CNRS, ISTerre, BP 53, F-38041 Grenoble CEDEX 9, France

*Corresponding author: agnese.fazio@uni-jena.de

Abstract – In small meteorite impacts, the projectile may survive through fragmentation; in addition, it may melt, and chemically and physically interact with both shocked and melted target rocks. However, the mixing/mingling between projectile and target melts is a process still not completely understood. Kamil Crater (45 m in diameter; Egypt), generated by the hypervelocity impact of the Gebel Kamil Ni-rich ataxite on sandstone target, allows to study the target-projectile interaction in a simple and fresh geological setting. We conducted a petrographic and geochemical study of macroscopic impact melt lapilli and bombs ejected from the crater, which were collected during our geophysical campaign in February 2010. Two types of glasses constitute the impact melt lapilli and bombs: a white glass and a dark glass. The white glass is mostly made of SiO_2 and it is devoid of inclusions. Its negligible Ni and Co contents suggest derivation from the target rocks without interaction with the projectile (<0.1 wt% of projectile contamination). The dark glass is a silicate melt with variable contents of Al_2O_3 (0.84-18.7 wt%), FeO_T (1.83-61.5 wt%), and NiO (<0.01-10.2 wt%). The dark glass typically includes fragments (from few µm to several mm in size) of shocked sandstone, diaplectic glass, lechatelierite, and Ni-Fe metal blebs. The metal blebs are enriched in Ni compared to the Gebel Kamil meteorite. The dark glass is thus a mixture of target and projectile melts (11-12 wt% of projectile contamination). Based on recently proposed models for target-projectile interaction and for impact glass formation, we suggest a scenario for the glass formation at Kamil. During the transition from the contact and compression stage and the excavation stage, projectile and target liquids formed at their interface and chemically interact in a restricted zone. Projectile contamination affected only a shallow portion of the target rocks. The SiO_2 melt that eventually solidified as white glass behaved as an immiscible liquid and did not interact with the projectile. During the excavation stage dark glass melt engulfed and coated the white glass melt, target fragments, and got stuck to iron meteorite shrapnel fragments. This model could also explain the common formation of white and dark glasses in small impact craters generated by iron bodies (e.g., Wabar).

Field Code Changed

1. Introduction

Impact melting is a common process occurring during meteorite impacts on solid bodies of the Solar System. On Earth, evidence of this process has been found as impact melt rocks (kilometer- to centimeter-scale) forming layered bodies in the crater or in the ejecta blanket, as dykes, veins, and vein networks (kilometer to centimeter-scale) in the crater basement, or as centimeter- to micrometer-sized masses and spherules in distal strewn fields called tektites and microtektites (e.g., Stöffler and Grieve, 2007; Osinski et al., 2013). Most impact melt rocks have been produced by large meteoritic impacts of projectiles more than tens of meters in diameter or larger. Impact melt rocks reflect the chemical composition of the target rocks; indeed the contribution of the projectile is typically lower than 1 vol%, because the projectile is mostly vaporized during large meteoritic impacts. Thus, the nature of the projectile can be detected only through the analysis of few geochemical fingerprints such as the distribution of siderophile elements (e.g., Cr, Co, Ni, and the platinum group elements), and or the isotope ratios of osmium and chromium (e.g., Koeberl et al., 2012; Goderis et al., 2013). During small impact events (final crater diameter < 1.5 km) the projectile contribution in melt rock can be high; the projectile survives to the impact and its partially melted beads and fragments can be found in the crater proximity (e.g., Kamil, 45 m in diameter; Wabar, largest crater 116 m in diameter; Henbury, 157 m in diameter; Aouelloul, 390 m in diameter; Barringer, 1.2 km in diameter). Nineteen out of 28 small impact craters were generated by the impact of iron or stony-iron projectiles (Earth Impact Database, accessed January 2016). Target rocks and iron projectiles have extremely different chemical compositions, thereby facilitating our understanding of the mixing-mingling processes between projectile and target.

In this paper, we present the results of petrographic and geochemical studies of impact melt lapilli and bombs from Kamil Crater (Egypt; Folco et al., 2010; 2011) in order to constrain the mechanism of formation of impact melt rocks in small terrestrial impact craters.

2. Background

Kamil is a simple, small impact crater (45 m in diameter and 10 m in final depth) with ejecta rays in southwestern Egypt (22°01’06’’N, 26°05’16’’E; Fig. 1). Discovered in 2008, an Italian-Egyptian geophysical campaign was organized in 2010 with the aim to conduct a geological and geophysical survey of the crater, a systematic collection of macroscopic meteorite specimens and microscopic impactor debris as well as an explorative sampling of macroscopic ejecta, including impact melt lapilli and bombs and target blocks (Folco et al., 2010 and 2011). The results of the geological and geophysical survey are reported in Urbini et al. (2012). The petrography and the

Field Code Changed

geochemistry of the iron meteorite Gebel Kamil are discussed in D'Orazio et al. (2011). The main petrographic and geochemical features of shocked and melted ejecta are presented in Fazio et al. (2014). The study of the microscopic impactor debris is reported in Folco et al. (2015). Based on archeological evidence the impact occurred less than 5,000 years ago (Folco et al. 2011). Thermoluminescence data from shocked target rocks provide an age interval between 2000 BCE and 500 CE (Sighinolfi et al. 2015).

2.1. Target rocks

Kamil Crater is located in a rocky desert area in the East Uweinat district in southwestern Egypt (Fig. 1). The impact of Gebel Kamil affected only the sedimentary rocks of the Gilf Kebir Formation, without involving the Precambrian crystalline basement, cropping out due northwest of the crater (> 150 m). In the crater area, the Gilf Kebir Formation consists of reddish brown sandstones with subhorizontal bedding topped by a ~1.3-m-thick bed of pale sandstones (Fig. 2). A loose soil mostly made of small, aeolian rounded crystals of quartz and sandstone pebbles locally cover the above stratigraphic sequence.

Pale and reddish brown sandstones are made of up to 98 vol% quartz; Fe-Ti oxides, tourmaline, and zircon are the most common accessory phases. Pale sandstones are coarse quartzarenite intercalated with medium-fine-grained wacke with siltstone levels. The matrix is mainly composed by kaolinite (Table 1), and its abundance increases with decreasing grain-size, ranging from negligible contents in coarse quartzarenite up to 40 vol% in medium-fine-grained wacke. Porosity is usually lower than 4 vol%. In coarse quartzarenite, pores are filled by syntaxial quartz cement. Reddish brown sandstones are very coarse- to coarse-grained, gritty and ferruginous quartzarenite. Iron oxides and hydroxides are important components of the matrix together with kaolinite (Table 1). The porosity of reddish quartzarenite is generally higher than that of pale sandstones (up to 24 vol%). Target sandstones from Kamil area show values of loss on ignition (L.O.I.) ranging from 0.65 to 3.91. These contents are mainly attributable to the presence of OH^- in the kaolinite of the matrix.

2.2. Projectile

Kamil Crater was formed by the hypervelocity impact of the iron meteorite Gebel Kamil. Gebel Kamil is an ungrouped ataxite (Ni = 20.6 wt%) characterized by a very fine-grained duplex plessite metal matrix (D'Orazio et al., 2011). Accessory minerals are schreibersite, troilite, daubréelite and native copper, in order of decreasing abundance. Thousands of meteorite fragments were found around the crater. They are all shrapnel in the <1 g to 34 kg mass range with the exception of a single regmaglypted individual of 83 kg.

Field Code Changed

The systematic visual search of specimens >10 g (D'Orazio et al., 2011) and the geomagnetic survey (buried shrapnel >100 g; Urbini et al., 2012) indicate that the minimum projectile mass is close to 5 t. However, the total mass of the Gebel Kamil meteorite is close to 10 t taking into account the estimate of the mass of shrapnel <10 g, buried shrapnel <100 g, and impactor debris fraction (Folco et al., 2015). This value is in agreement with estimates of its pre-atmospheric mass, namely >20 t, most likely 50-60 t (Ott et al., 2014). The absence of companion craters suggests that Gebel Kamil meteorite impacted the ground as a single mass or a very tight cluster of fragments, and that it underwent only minor fragmentation and separation during atmospheric flight (Folco et al., 2010 and 2011).

2.3. Ejecta

A radial pattern of ejecta characterizes Kamil Crater up to ~300 m from crater rim (Fig. 1, and Fig. 2 in Urbini et al., 2012). Ejecta consists mainly of shocked and unshocked sandstone blocks, plus meteorite shrapnel, and impact melt lapilli and bombs. The bulk of the ejecta is preferentially concentrated in sector spanning clockwise from the north to the southwest, indicating that the projectile arrived from NW. Within ~50 m from the crater rim unshocked sandstone clasts and impact melt lapilli and bombs are more common; further away, the shocked sandstone clasts dominate.

Shocked sandstone blocks show several metamorphic features including fracturing, planar deformation features (PDFs) in quartz, high-pressure SiO_2 polymorphs, melt veins, and melt in possible shatter cones (Fazio et al., 2014). Some of these features have never been reported before from impact craters of comparable size. Shock metamorphic and melting features in the target indicate peak pressure between ~30 and ~60 GPa, and impact velocities of 3.5–5.5 km s^{-1} for vertical impact or 5.0 – 7.5 km s^{-1} for an impact angle of 45° (Fazio et al., 2014).

Impact glass lapilli and bombs comprise two types of glasses: a white glass (Figs. 3a and 3b) and a dark glass (Figs. 3c and 3d; Table 2). Dark glass is gray-green in color, magnetic, and contains several target fragments, whereas white glass is milky white to light gray in color, non-magnetic, and nearly clast free (Folco et al., 2010; Fazio et al., 2014).

3. Analytical Methods

The petrographic study of the impact melt lapilli and bombs was carried out by optical and electron microscopy observations. Optical microscope Zeiss Axioplan and Scanning Electron Microscope (SEM) Philips XL30, operating at 20 kV and coupled with an energy-dispersive X-ray fluorescence spectrometer (EDX), were used at Pisa University's Dipartimento di Scienze della Terra (Italy). Field Emission Scanning Electron Microscope (FE-SEM) Jeol JSM 6500F (upgraded

Field Code Changed

to 7000 series), operating at 10 kV, was used at the Istituto di Geofisica e Vulcanologia (INGV) of Rome (Italy).

The chemical analyses of glasses and minerals were obtained by electron microprobe. For the analyses of the dark and white glasses, we used the electron microprobe Jeol JXA 8230 fitted with five wavelength dispersive spectrometers at the Institut des Sciences de la Terre (ISTerre) of Grenoble (France). Running conditions were 15 kV accelerating voltage, 12 nA beam current and 1 µm nominal beam spot. The ZAF procedure was employed for raw data reduction. Standards used for instrumental calibration were SiO_2-rich glass (USNM 72854), ilmenite (USNM 96189), and hornblende (USNM 143965). Average detection limits are 0.04 wt% for Na_2O and ZrO_2; 0.02 wt% for Al_2O_3, Cr_2O_3, and V_2O_3; and 0.01 wt% for MgO, CaO, K_2O, FeO, MnO, TiO_2, NiO, and P_2O_5.

For the analyses of the Ni-Fe metal blebs embedded in glass, we used the electron microprobe Cameca SX50 fitted with four wavelength dispersive spectrometers at the Istituto di Geoscienze e Georisorse (IGG) of the Consiglio Nazionale delle Ricerche in Padova (Italy). Running conditions were 15 kV accelerating voltage, 20 nA beam current and 1 µm nominal beam spot. The manufacturer-supplied PAP procedure was applied for raw data reduction. Standards used for instrumental calibration were natural minerals (diopside, apatite, and sphalerite), and pure elements (Fe, Ni, and Co). Average detection limits are 0.04 wt% for S, 0.08 wt% for Fe, Co, Ni, and Si, and 0.11 wt% for P.

Whole-rock major elements of unshocked target materials and impact melt lapilli and bombs from Kamil Crater were determined on glass beads by X-Ray Fluorescence (XRF; ARL 9400 XP spectrometer) at Pisa University's Dipartimento di Scienze della Terra (Italy), using the procedure described by Tamponi et al. (2003). Detection limits are <0.01 wt% for all major-element oxides. Average precisions are better than 2% (relative standard deviation = 1 x standard deviation/average*100) for oxides concentrations >1 wt% and better than 8% for oxide concentrations between 1 and 0.1 wt%.

Inductively coupled plasma-mass spectrometry (ICP-MS; Perkin-Elmer NexION 300x) was used to determine the concentrations of V, Cr, Ni, Co, Cu of target rocks and impact melt lapilli and bombs. Analyses were carried out at Pisa University's Dipartimento di Scienze della Terra. Samples were dissolved with a mixture of concentrated HF + HNO_3 following an improved version of the protocol described in D'Orazio (1995). Detection limits are about 0.1 µg g^{-1} for Co, 0.5 µg g^{-1} for Ni, Cr and V, and 1 µg g^{-1} for Cu. At the concentration levels of the studied samples analytical precision varies between 5 and 10 % (relative standard deviation). The accuracy of the data was checked against a number of geochemical reference materials including BIR-1, RGM-1, W-2, WS-E, PM-S, and are generally better than 10%.

Field Code Changed

4. Results

4.1. White glass

Impact melt lapilli and bombs made of white glass can be classified as vesicular clast-poor to clast-free impact melt rocks, according to the classification scheme proposed by Stöffler and Grieve (2007) and Osinski et al. (2013). At hand-specimen scale, they generally appear white or light gray (Figs. 3a and 3b). Some masses are similar to volcanic pumice (Fig. 3a), with rounded vesicles (up to ~30 vol%) ranging from few tens of micrometers to few millimeters. Several, impact melt lapilli and bombs made of white glass are coated by dark glass (Fig. 3b).

In thin section, the white glass is generally colorless (Fig. 4a), and backscattered-SEM images show that its composition is homogenous (Fig. 4b). The bulk composition of the white glass typically consists of ~100 wt% SiO_2 (Tables 3). Bulk samples M23 and L04 that are not coated by dark glass, have less than 0.5 wt% FeO_T and less than 0.7 wt% Al_2O_3. Their Ni and Co concentrations (Ni = 34 and 18 µg g^{-1}, Co =1.8, and 1.2 µg g^{-1}, respectively; Table 3) are of the same order of magnitude of the target rocks (Ni = 6.9 - 13 µg g^{-1} and Co = 0.5 - 10 µg g^{-1}; Table 1). Petrographic investigation and EPM analyses show that white glass consists of vesicular homogeneous lechatelierite (Fig. 4; Table 4). Bulk sample L03 and L08 that are coated by dark glass (Fig. 3b), have significant concentrations of FeO_T (~ 0.8 wt%), Ni (121 – 233 µg g^{-1}), and Co (7 – 11 µg g^{-1}).

Amorphous quartz grains, i.e., diaplectic quartz glass (Table 4), with sporadic birefractive domains were found embedded in lechatelierite in sample L09. Under the SEM, birefractive domains may show multiple sets of planar to subplanar bands of amorphous silica material with micrometric spacing (Fig. 5a), often associated with tiny vesicles. In Fig. 5b, a bright 1 µm-in-size object is observed. EDX-SEM analysis indicates that it is composed of 100 wt% SiO_2. Due to its brightness, we suppose that it is a high-pressure polymorph of SiO_2. The occurrence of surrounding radial fractures propagating in the host phase indicates a transformation from a phase with a small molar volume to a phase with a higher molar volume (e.g., from stishovite to coesite). These objects are quite common in former quartz grains almost completely substituted by amorphous SiO_2 in sample L09.

Shocked quartz grains show distinct types of contacts with the surrounding lechatelierite. The contact with birefringent grains is characterized by a distinct boundary marked by small elongated vesicles/cracks on the lechatelierite side (Fig. 5c). These vesicles/cracks are geometrically arranged, parallel to the contact, and their size decreases approaching the contact. Their arrangements could be a memory of the crystallographic planes of former quartz crystals. The

Field Code Changed

contact with diaplectic quartz grains is gradual and decorated by roundish vesicles decreasing in size approaching the quartz grain (Fig. 5d).

Rare zircon grains, partially decomposed into baddeleyite (ZrO_2) plus SiO_2, were found in shocked clasts or floating in lechatelierite (Fig. 6a). Sparse pockets and veinlets of Fe-rich, Ni-free silicate glass were also locally found in lechatelierite (Fig. 6b). They generally show liquid immiscibility textures. Figure 6c features a thin (few micrometers) veinlet surrounded by finely dispersed micro- to nanoblebs. In this glass, FeO_T, varies between 58.8 wt% and 80.3 wt%, and SiO_2 between 8.24 wt% and 37.1 wt% (Table 4). CaO and MgO are respectively the third and the fourth most abundant component of this melt, varying between 0.19 - 5.22 wt% and 0.03 - 3.97 wt%, respectively (Table 4).

4.2. Dark glass

Impact melt lapilli and bombs made of dark glass are vesicular clast-rich impact melt rocks with scoriaceous textures (Fig. 3c), according to the classification scheme proposed by Stöffler and Grieve (2007) and Osinski et al. (2013). The dark glass occurs as isolated gray-green masses, as well as coatings of the white glass impact melt lapilli and bombs (Fig. 3b), and as small masses (mm- to cm-sized) stuck on the surfaces of iron meteorite fragments (Fig. 3d). The bulk composition of the dark glass (sample L06; Table 3) has significantly higher concentrations of FeO_T (14.6 wt%), Al_2O_3 (5.8 wt%), Ni (2.3 wt%), and Co (908 μg g^{-1}) than white glass.

In thin section, the dark glass is usually transparent and old-yellow to brown in color, rarely opaque (Figs. 4a and 7a). Vesicles are commonly micrometric and roundish; yet irregular vesicles up to 5 mm also occur. Dark glass contains abundant variably shocked target fragments (Figs. 7a and 7b), mainly shock metamorphosed quartzarenite clasts, amorphous silica and lechatelierite inclusions, and projectile materials mainly in form of Ni-Fe metal blebs (Fig. 7b).

Target fragments are, in order of abundance, clasts up to 5 mm in size of shocked sandstone, clasts up to 1 mm in size of diaplectic quartz glass and lechatelierite (Figs. 7a and 7b). Target inclusions are generally monotypic clasts.

Quartz crystals in shock metamorphosed quartzarenite clasts, typically some hundred micrometers in size, may show strong undulose extinction and planar fractures, PDFs (Fig. 7c, inset) as well as multiple sets of planar to subplanar bands of amorphous silica material with micrometric spacing (Fig. 7c). Quartzarenite grain size never exceeds 700 μm. As showed by Fazio et al. (2014), the most common crystallographic orientations of the PDFs are $\{10\bar{1}3\}$ and $\{11\bar{2}2\}$ amounting to 17%, followed by $\{10\bar{1}1\}$, 15%, indicating formation under shock pressures between

Field Code Changed

10 and 20 GPa. Intergranular glass occurs in the interstices of shocked quartz grains. The chemical composition of shocked quartz grains is reported in Table 5.

Several target inclusions consist of diaplectic quartz glass Figs. 7a and 7b). They are roundish, exclusively (or nearly so) made of SiO_2, devoid of vesicles, low relief, always (or nearly so) extinct under crossed polars, and devoid of any particular internal structures like, for instance, schlieren. Diaplectic quartz glass may contain bright micrometric objects made of SiO_2 as those seen in the shocked sandstone clasts embedded in the white glass (Fig. 5b). Although target inclusions display shock features typical of different shock pressure regimes, they are found very close one to another and they do not show any preferential distribution in the dark glass (e.g., Fig. 7b).

Projectile materials within the dark glass are represented by common Ni-Fe metal blebs and rare fragments, up to 200 µm in size, of the Gebel Kamil iron meteorite (Figs. 3c and 7b). Nickel-Fe metal blebs can reach the maximum size of 200 µm (Fig. 7d) and show fractal size distribution down to the µm-to-nm-scale (e.g., Fig. 7e). Blebs larger than 10 µm are nearly spherical and are made of rounded Ni-Fe metal particles (cellular intergrowth texture). The interstitial space between the metal particles is filled by P-rich (darker) and S-rich (lighter) materials (Fig. 7d). Often P-rich material forms a rind separating the metal blebs from the enclosing glass. The chemical composition of Ni-Fe metal blebs of sample L06 is quite homogenous: Ni is between 60.3 wt% and 69.8 wt% (the percent Relative Standard Deviation, RSD% = 6%), Fe is between 28 wt% and 36 wt% (RSD% = 11%) and Co is between 1.56 and 1.95 wt% (RDS% = 8%; Table 6). There is no correlation between Ni content and diameter of the Ni-Fe metal blebs. Fig. 8 shows that Ni-Fe metal blebs from the dark glass have higher Ni content than Gebel Kamil and most of the Ni-rich spherules found in microscopic impact melt beads from the soil surrounding Kamil (Folco et al., 2015).

The contact between dark glass and shocked sandstone clasts is rather complex (Fig. 7e). The quartz grain is surrounded by vesicular lechatelierite. Lechatelierite and adjacent dark glass show an interfingered contact indicating coexistence and immiscibility of the silica and dark glass melts. Few µm away from the contact, the dark glass shows fine immiscibility textures given by sub-micrometric lechatelierite blebs floating in dark glass. These textures give a mottled appearance to the dark glass when seen at relatively low-magnification in BSE images (upper part of Fig. 7e). At higher magnification the blebs are better discriminated (Fig. 7f).

Thin envelopes (up to 100 µm thick) of opaque dark glass may occasionally surround target rock clasts and vesicles, or mark the edge of the sample. Opaque dark glass is decorated by

Field Code Changed

crystallites of Fe-oxides (Fig. 7g). Fig. 7g features a few µm-thick Ni-rich melt occurring at the edge of sample L06.

Electron microprobe analyses of the dark glass show a great variability in Si, Al, Fe and Ni contents (Table 5). In sample L06, Al_2O_3, FeO_T, and NiO are between 0.8-18.7 wt%, 1.8-61.5 wt%, and <0.01-10.2 wt%, respectively. Some analyses show anomalous high P_2O_5 values (up to 15.5 wt%). The opaque dark glass featured in Fig. 7g. contains the highest Fe and Ni contents (FeO_T 61.5 wt%; NiO 10.2 wt%). The dark glass coating in sample L03 tends to have higher SiO_2 (~60 wt%) and lower FeO_T and NiO contents (<20 wt% and < b.d.l., respectively). In dark glass, Al_2O_3 contents increase with increasing of FeO_T contents and with decreasing of SiO_2 contents (up to SiO_2 ~50 wt%). Quartz and lechatelierite inclusions in dark glass and dark glass form an almost continuous trend in the diagram Si (wt%) vs Fe (wt%) (Fig. 9).

5. Discussion

5.1. White glass: a virtually pure target melt

Major- and trace-element compositions indicate that the white glass is a nearly pure melt of the target sandstone rocks. Its nearly pure silica composition and, in particular, its very low Al_2O_3 and FeO_T contents (bulk analyses Al_2O_3 < 0.7 wt% and FeO_T < 0.4 wt%, Table 2; spot analyses Al_2O_3 < 0.3 wt% and FeO_T < 0.3 wt%, Table 3), suggest that the pale quartzarenite with negligible matrix (bulk analysis Al_2O_3 = 0.3 wt% and FeO_T = 0.1 wt%; Table 1) is the most plausible protolith for the impact melt lapilli and bombs made of white glass. The constituent lechatelierite of the white glass indicates melting temperatures in excess of 1700 °C. The bulk compositions of samples L03 an L08 have higher FeO_T, Ni, and Co contents (L03: 0.77 wt% FeO_T, 121 µg g^{-1} Ni, and 7 µg g^{-1} Co; L08: 0.84 wt% FeO_T, 233 µg g^{-1} Ni, and 11 µg g^{-1} Co; Table 3) indicating some contamination with their dark glass coatings.

The bulk chemical composition of the impact melt lapilli and bombs and target rocks from Kamil are plotted in the diagrams Fe vs Ni and Co vs Ni (Fig. 10). All the white glass samples (including those coated by dark glass) have Ni/Fe and Ni/Co ratios (Table 3) significantly lower than Gebel Kamil (Gebel Kamil: Ni/Fe = 0.26 and Ni/Co ~30; Fig. 10). Based on Ni and Co concentrations of these samples and of the impactor, the projectile contamination of the white glass is less than 0.1 wt%.

In white glass impact melt lapilli and bombs, additional examples of mineral shock and melting can be found. Accessory minerals within target rocks of the Kamil area represent about 1-2 vol%. They are Fe-Ti-oxides, tourmaline and zircon (Fazio et al., 2014). Depending on their melting temperatures, these minerals can melt or be shocked within impact melt glass. For example,

Field Code Changed

a single partially decomposed zircon crystal was found within the white impact melt bomb M23 (Fig. 6a). The partial decomposition of zircon into SiO_2 and ZrO_2 (baddeleyite) indicates post-shock temperatures in excess of 1676 °C followed by the rapid quenching of the glass (Wittmann et al., 2006). Mineral melting of a polymineralic rock produces melts with physical properties (particularly viscosity), limiting or preventing their mixing. In a context characterized by rapid heating up to extreme temperature followed by rapid cooling, mineral melting may thus produce shock melts with immiscibility textures. For instance, in samples L08 and L04, Fe-rich, Ni-free and Fe-Ca-Mg-rich Ni-free silicate melts form of network of veinlets, micro- to nanoblebs (Figs. 6b and 6c). The chemical composition of the Fe-rich Ni-free melts (Table 4) could be explained by an important contribution from tourmaline and iron oxides (Table 4).

The shocked quartzarenite clasts embedded in white glass L09 are interpreted as impact melt relicts. They result from the incomplete melting of quartzarenite grains and subsequent rapid quenching of the target melt (Fig. 5). In general, melting usually starts in correspondence of rock heterogeneities, where it is possible to reach a local enhancement of pressure and temperature (e.g., Güldemeister et al., 2013), or in correspondence of mineral phases with lower melting temperatures, typically concentrated in the matrix. In target quartzarenite melting likely started in the matrix to then involve quartz grains. Due to rapid quenching, the rocks did not reach total melting leaving behind highly shocked quartz grains, made of variable proportions of amorphous silica and crystalline domains. The relatively abundant diaplectic quartz glass in sample L09 indicates that the maximum temperature reached to melt this sample was lower than 1515°C, which is the disequilibrium melting temperature of β-quartz (Petzold and Hinz, 1976). All this is consistent with evidence from MEMIN project's laboratory-scale experiments (e.g., Ebert et al., 2013), thereby supporting the validity of such experiments to reproduce at least natural small-scale impacts produced by iron meteorites.

Shocked quartz grains from metamorphosed target rocks and impact melts from Kamil Crater studied by Fazio et al. (2014) and in this work, respectively, provide information on the role of PDF in the melting of target sandstone. The a-to-d image sequence in Fig 11 shows shock features in quartz grains which experienced increasingly stronger shock. Fig. 11a features a quartz grain with multiple (three) sets of PDFs. Fig. 11b features a quartz grain with multiple sets of planar to subplanar bands of amorphous silica material with micrometric spacing, abutting silica glass pockets; note the lack of a contact between the material in the bands and that in the pockets indicating a continuum. Fig. 11c shows a quartz grain with multiple sets of subplanar bands of amorphous silica material with greater thickness than in Fig. 11b; Fig. 11d shows a detail of a quartz grain in which the subplanar bands of amorphous silica material are so thickened that this

Field Code Changed

material dominates the original crystal volume. The increasing amount of the amorphous silica material in the planar to subplanar bands indicates i) increasing melting degree of the quartz grains and ii) preferential melting development along PDFs, i.e., from preexisting amorphous material in the shocked quartz crystals. The four images shown in Figure 11 are, thus, a sequence of snapshots of the impact melting process of quartz under strong shock; an analogous process was modeled by Stöffler and Langenhorst (1994). Different melting degrees could be found in the same sample indicating once more that shock pressure could be heterogeneously distributed at the millimeter to micrometer scale (Kowitz et al., 2013). Note also that the multiple sets of planar to subplanar bands of amorphous silica material in shocked quartz grain have been described in literature (e.g., Fig. 5a (Qtz-B) in Ebert et al., 2013). In line with the present interpretation, we propose to call these features as "melted relict PDF".

5.2. Dark glass: a mixture of target and projectile melts

Due to its high Fe and Ni contents, the dark glass has two precursors: Kamil target rocks and the iron meteorite Gebel Kamil (Tables 1, 5, and 6). The high Al content of dark glass suggests that the target protolith was the pale wacke with siltstone levels (Table 1 and 3). The Ni/Fe (0.20) and Ni/Co (25.3) ratios of sample L06 are the closest to Gebel Kamil (Ni/Fe = 0.26 and Ni/Co = ~30; Folco et al., 2015). The Ni and Co enrichments of the dark glass of sample L06 (Fig. 11) are compatible with a projectile contamination of ~11-12 wt%, i.e. much higher than what observed in white glass (<0.1 wt%). Barringer glasses and Wabar glasses also show different percentage of projectile contamination. The glasses from Barringer crater described by Hörz et al. (2002) show a range of meteoritic component from ~5 wt% to 15-20 wt%. Wabar glasses are divided, similarly to Kamil glasses, into white and black or dark glasses. The projectile contamination of the white glass is less than 1 wt% (Hörz et al., 1989; <0.1% for Kamil white glass, see previous section). Instead, the projectile contamination of black glass masses larger than 1 cm in size is ~4 wt% (Hörz et al., 1989) and of black glass particles smaller than 1 cm in size is generally >10 wt% (Mittlefehldt et al., 1992).

The electron microprobe analyses of dark glass show an almost continuous mixing trend between SiO_2 phases (quartz and lechatelierite) and the projectile (Fig. 9a). Due to the occurrence of clay minerals matrix in Kamil target rocks, the dark glass compositions from Kamil are slightly shifted to the left hand side of the mixing curve, i.e., toward kaolinite composition (Fig. 9a). This trend is the same followed by microparticles found in Kamil soil (Fig. 9b; Folco et al., 2015) and by glass produced experimentally by shooting a projectile made of Campo del Cielo iron meteorite against a quartz-rich sedimentary target (Fig. 9b; Seeberger Sandstein; fine-grained sandstone ~89

Field Code Changed

vol% quartz and ~10 vol% of phyllosilicate; porosity ~23 vol%; MEMIN Project; Ebert et al., 2013). The Fe-Ni-richest glass localized at opaque borders (Fig. 7g) recalls the black-rimmed margins around large glassy target fragments described by Hamann et al. (2013) for the Wabar glass. Some analyses of the dark glass show a moderate enrichment in TiO_2 (up to 2 wt%), indicating that also accessory Fe-Ti oxides contributed to the chemical composition of the dark glass, hence also a minimal part of the Fe of the dark glass could have a terrestrial origin (Fig. 10a).

Liquid immiscibility textures are very common in the dark glass from Kamil (Figs. 7e and 7f), most notably those consisting of lechatelierite blebs in the dark glass. These textures, also called emulsion textures, formed for the difficulty in completely mixing a highly polymerized, SiO_2-rich melt and a poorly polymerized FeO-rich silicate melt. Similar immiscibility textures also occur in the Wabar black glass (Hamann et al., 2013). This is further evidence that liquid immiscibility is a common and important process in impact glass formation, particularly in small impact events in which peak temperature is immediately followed by extremely rapid quenching (seconds to few minutes).

Petrographic observations also confirm that the dark glass is the result of the interaction between the target and the projectile. Target fragments within the dark glass are very common; they are generally monotypic inclusions of shocked sandstone clasts, diaplectic glass, and lechatelierite fragments. They are randomly dispersed in the dark glass (Figs. 1c, 7a and 7b). They represent three different regimes of shock metamorphic pressures: PDFs in shocked sandstone clasts, 10-20 GPa (Fazio et al., 2014); diaplectic glass, >35 GPa (Stöffler and Langenhorst, 1994); lechatelierite, 50-60 GPa (Stöffler and Langenhorst, 1994).

Two possible mechanisms can explain the occurrence of target fragments within the dark glass: (i) target fragments are corroded yet undigested relicts of the process of melting and mixing involving target and projectile during the end of contact and compression stage; (ii) target fragments were engulfed by the dark glass during the excavation stage while still hot and liquid. The first mechanism is similar to that described in the previous section to explain the occurrence of quartz relicts in sample L09. This mechanism is thought to be the most plausible to explain the occurrence of target inclusions within the experimentally produced dark glass by Ebert et al. (2013; 2014). An evidence of this mechanism could be represented by the occurrence of lobated margins of silica glass inclusions within dark glass (Fig. 7e). This type of margin is indicative of a high temperature process. The second mechanism could explain more easily the occurrence of dark glass coatings of centimeter-size white glass masses (Fig. 3b) and microparticles of target materials, both consisting of lechatelierite and shocked quartz clasts (Fig. 4 and Folco et al., 2015). Most of the microparticles studied by Folco et al. (2015) show degassing microstructures on their external

Field Code Changed

surfaces like bubbles and hollows indicating that these particles were still molten when in air during ejection. White glass masses coated by dark glass were also described at Wabar (e.g., Mittlefehldt et al., 1992; Hörz et al., 1989), Barringer (e.g., Nininger, 1954). Impact melt coatings are also reported in lunar samples (e.g., Apollo 16 lunar samples; Grieve and Plant, 1973).

The enrichment in Ni relative to Fe of the Ni-Fe metallic blebs (up to 200 µm in diameter) commonly found in the dark glass compared to Gebel Kamil derives from the different redox properties of these two elements. Iron is preferentially oxidized relative to Ni, because the Gibbs free energy variation ($\Delta G^0_{Fe/FeO}$) of the reaction of oxidation of Fe ($Fe + 0.5\ O_2 = FeO$) is lower than $\Delta G^0_{Ni/NiO}$ of the reaction of oxidation of Ni ($Ni + 0.5\ O_2 = NiO$). Moreover, the partition coefficient between a metallic and a silicate melt of Ni is higher than that of Fe ($D_{Ni\ met/sil} >> D_{Fe\ met/sil}$; e.g., Righter et al., 1997). For these reasons, the silicate liquid is enriched in Fe, and the metallic liquid is enriched in Ni. We thus propose that the Ni-Fe metallic blebs result from the chemical fractionation of the metallic liquid of the projectile. Metal blebs were described in several impactites (e.g., Wabar (Saudi Arabia), Gibbons et al., 1976; Hamann et al., 2013; Monturaqui (Chile), Bunch and Cassidy, 1972; Gibbons et al., 1976; Henbury (Australia), Gibbons et al., 1976; Barringer Crater (Arizona) Kearsley et al., 2004) and in impact experiments (Ebert et al., 2013; Ebert et al., 2014). Metal blebs from these impact craters are also enriched in Ni, and show a wide range of chemical composition: from values comparable to their iron meteorite impactor (Ni = 8 wt%, 20 wt%, and 13 wt% for Wabar, Henbury, and Monturaqui, respectively; Gibbons et al., 1976) up to very high Ni concentration (Ni = 64 wt%, 94 wt%, and 75 wt% for Wabar, Henbury, and Monturaqui, respectively; Gibbons et al., 1976). The P-rich and S-rich material, occurring in the interstices and as rind of Fe-Ni metal particles forming the metal blebs, represent the residual liquid of the process of crystallization/quenching of the molten meteoritic liquid depleted in Fe into rounded Ni-Fe metal particles (bulk P and S contents of Gebel Kamil are 0.04 wt% and 0.02 wt%, respectively; Gemelli et al., 2015). Similar metal bleb textures were also described by Bunch and Cassidy (1972) for the Monturaqui impactites and by Kearsley et al. (2004) for the Barringer Crater impactites.

5.3. Impact melting scenario

The model for the formation of the impact melts at Kamil is based on the geochemical and petrographic evidence discussed in the previous paragraphs, on the study of the microparticles scattered in the soil around the crater (Folco et al., 2015), on the recent model proposed by Ebert et al. (2014), and on the widely accepted general model for impact cratering (e.g., Osinski and Pierazzo, 2013). Furthermore, it reasonably assumes that present-day field situation was similar to

Field Code Changed

that at the time of the impact <5,000 years ago given that present-day hyperarid conditions were established since 5,000 years (Kuper and Kröpelin, 2006).

Impact cratering is a process characterized by strong disequilibrium. The duration of impact events the size of Kamil is supposed to be very short, on the scale of few seconds. The contact and compression stage starts when the projectile reaches the target surface and penetrates in it for 1-2 times its diameter (Osinski and Pierazzo, 2013). At the contact point the maximum shock pressure is reached, i.e. at least of 30-60 GPa according to Fazio et al., 2014, most likely around 50 GPa due to the low porosity (0-4 vol%) of the target rocks (Wünnemann et al., 2008). Based on planar impact approximation (Melosh, 2013), this range of shock pressures corresponds to impact velocities between 5.0 km s^{-1} (30 GPa) and of 7.5 km s^{-1} (60 GPa), assuming an impact angle of 45° (Fazio et al., 2014). During this stage, the kinetic energy of the projectile is converted into heat and shock waves propagating both in the target and in the projectile (Fig. 12a; Osinski and Pierazzo, 2013). Shock pressure rapidly decreases from pressures of the order of 30-60 GPa at the contact point down to pressures < 1GPa at the crater wall (Fig. 12a).

According to Ebert et al. (2014), between the contact and compression stage and the excavation stage there is an intermediate stage, which is the most important for the impact melt formation and for the physical-chemical interaction between the target and the projectile. This intermediate stage is indicated in Figs. 12a and 12b as "end of contact and compression stage". During this intermediate stage, the projectile is intensely plastically deformed, as evidenced by the shear bands observed in fragments of the Gebel Kamil meteorite (D'Orazio et al., 2011), as well as in experimental analogs (Kenkmann et al., 2013b). A rarefaction wave, produced by the reflection of the shock wave at the rear surfaces of the projectile, moves downward through the projectile and then through the target. This propagation produces decompression, heating, melting of the target and the projectile (Fig. 12b; Stage II in Ebert et al., 2014), and eventually the ejection of meteorite shrapnel and target fragments in the excavation stage.

At Kamil, both the projectile and target rocks melt along their interface during the above intermediate stage (Figs. 12b and 12c). Here, before ejection, the melt from the projectile is injected into the melted target rocks. Impact melting of the target originally produces two silicate melts reflecting the heterogeneity of the source rocks, i.e., the pale sandstone bed (~1.3 m thick) at the top of the sedimentary sequence observed in the crater rim (Fig. 2). This consists of intercalated quartzarenite and wacke with siltstone levels whence a silica melt and a silicate melt enriched in Al formed, respectively. The silica melt did not geochemically interact with the projectile melt and eventually gave rise to the white glass. Interaction did not occur because the high degree of polymerization of the SiO_2 glass prevented mixing with a FeO-rich liquid. Furthermore, the smaller

Field Code Changed

the crater, the shorter is the time for melts homogenization (Hörz et al., 1989). In turn the Al-rich silicate melt did interact (mixing, fractionation) with projectile melts, producing a silicate glass rich in Al and Fe and containing numerous Ni-Fe metallic blebs. Geochemical interaction occurred because a Al_2O_3-rich silicate liquid has a relatively low degree of polymerization and therefore, it could mix with the oxidized melt from the projectile. This mixed melt eventually gave rise to the dark glass (Figs. 7 and 9). Nickel-Fe metallic blebs are enriched in Ni and represent the residue of the projectile melting under oxidizing conditions (Fig. 7d). Note that impact melting of target rocks at Kamil Crater thus involves only the first 1 m or so of the stratigraphic sequence. Shocked sandstone clasts in the target melts include pale sandstone clasts only. So far in our investigations, ferruginous sandstone clasts have not been observed. The projectile-target interaction zone has a very small volume compared to the total volume of rocks affected by the impact (Ebert et al., 2014). Hence, melted and shocked rocks formed just below this zone had a negligible interaction with the projectile melt (Fig. 12c).

Ejection during the subsequent excavation stage (Fig. 12c) is the final consequence of the passage of the rarefaction wave: the ejection starts form the rear surface of the projectile proceeding into the projectile and then into the target (Langenhorst and Deutsch, 2002). Highly deformed projectile fragments are the first objects ejected. They are followed by still hot and plastic masses of dark and white glass and then of fragments of target rocks variously shocked (Fig. 12c). Ejection is a chaotic and rapid stage and it is likely that a significant mechanical interaction between impact melt glasses and target and projectile fragments occurred during this stage, producing the engulfment of target fragments of various sizes and shock degrees into the dark glass (Figs. 1c, 6, and 7; Folco et al., 2015) and the sticking of the dark glass onto meteorite shrapnel fragments (Fig. 1d). Due to the high temperature of the system, minor local chemical interaction at the contact between the dark glass and the inclusions could also have occurred.

6. Summary and conclusions

Impact melt lapilli and bombs from Kamil crater (45 m in diameter) represent an invaluable natural material for the study of impact melting process and target-projectile chemical-physical interaction in small terrestrial impact craters. The hypervelocity impact of the Gebel Kamil iron meteorite onto sandstone target rocks produced two types of glasses occurring in the area as ejected impact melt bombs and lapilli: the white glass and the dark glass. The white glass is highly vesicular and almost exclusively made of SiO_2, i.e. lechatelierite, and contains shocked sandstone clasts, although rarely. Its liquid formed from the melting of the quartzarenite portions of the topmost pale sandstone layer of the target stratigraphic sequence. The dark glass is the solidification

Field Code Changed

product of a silicate melt with variable contents of Al_2O_3 (0.84-18.7 wt%), FeO_T (1.83-61.5 wt%) and NiO (<0.01-10.2 wt%). The dark glass typically includes fragments (from few μm to several mm in size) of shocked sandstone, diaplectic quartz glass, lechatelierite, and Ni-Fe metal spherules. The dark glass formed by mixing of projectile melt and a target Al-rich silicate melt. The latter derived from the melting of the Al-rich wacke with siltstone levels intercalated with quartzarenite in the topmost pale sandstone layer of the target stratigraphic sequence. The whole mass of impact melt at Kamil crater thus derives from the melting of the first ~1 m of the target stratigraphic sequence. Based on Ni and Co concentrations, the dark glass contains about 11-12 wt% of projectile material. In the context of a small impact characterized by rapid melting and quenching, the SiO_2 liquid of the white glass did not interact with the projectile melts due to its high degree of polymerization. The mixing of the target silicate Al-rich with the projectile melt was likely possible due to the lower polymerization of the Al-rich silicate melts. Ni-rich metal blebs in dark glass are indicative of Fe fractionation into the host melt under oxidizing conditions. Melting and mixing/mingling of the target and projectile occurred at their interface at the end of the contact and compression stage. The interaction zone is supposed to have a very small volume compared to the total volume of rocks affected by the impact (up to ~1 m).

The target inclusions in dark glass could be either relicts of the precursor rocks that suffered shock melting entrained in the glass at the contact interaction zone, or target fragments engulfed by the dark glass during the excavation stage. This latter process was dominantly mechanical, even though minor and local chemical high temperature interactions could have occurred at the contact between the dark glass and the inclusions in the ejecta curtain. During the excavation stage, still hot masses of dark glass could stick onto iron meteorite shrapnel in the ejecta curtain.

In general, evidence from Kamil Crater shows that in small impact craters down to few tens of m in diameter:

i) Impact melting does occur and involves both the projectile and the target.

ii) Impact melting involves surface rocks less than very few meters in depth and thus small volumes up to few tens of cubic meters.

iii) Impact melting is dominated by strong disequilibrium due to the rapid heating and rapid quenching from high temperatures. Immiscibility may play an important role, as in the case of target silicate melts with variable polymerization.

iv) Oxidation during iron projectile melting favors its mixing with low-polymerization target silicate melts.

Most of our data about the physical-chemical interactions during impact melting at Kamil Crater are consistent with those obtained in analog hypervelocity impact cratering experiments by

Field Code Changed

the MEMIN project (Kenkmann et al., 2013a; Ebert et al., 2014), validating their experimental set up and results at least for small-scale impacts generated by iron meteorite bodies.

Acknowledgements – This work was supported by the Italian Ministero degli Affari Esteri - Progetti di Grande Rilevanza, Protocollo Esecutivo ITALIA-EGITTO. The 2010 geophysical expedition work was carried out within the framework of the 2009 Italian-Egyptian Year of Science and Technology. We thank Prof. M. Alsherbiny (former President of the Egyptian National Academy for Scientific Research and Technology) and Prof. F. Porcelli (Scientific Attaché, Italian Embassy, Egypt) for diplomatic and institutional support; the Egyptian Army for logistical support. Agnese Fazio is supported by the University of Pisa PhD School on Earth Science Scuola di Dottorato in Scienze di Base Galileo Galilei, and by the Barringer Family Fund for Meteorite Impact Research 2014. Luigi Folco and Massimo D'Orazio are also supported by the University of Pisa Fondi di Ateneo. Institut des Sciences de la Terre (ISTerre) of Grenoble is part of Labex OSUG@2020 (ANR10 LABX56). The authors are grateful to Valentina Batanova, Andrea Cavallo, Raul Carampin, and Gabriele Paoli for their assistance during electron microprobe analysis at ISTerre (Grenoble), field emission scanning electron microscope analysis at INGV (Rome), electron microprobe analysis at CNR-IGG (Padova), and ICP-MS analysis (Pisa), respectively. Christian Koeberl and Birger Schmitz, and an anonymous reviewer are acknowledged for their constructive reviews.

References

Bunch T. E. and Cassidy W. A. (1972) Petrographic and electron microprobe study of the Monturaqui impactite. *Contrib. Mineral. Petrol.* **36**, 95–112.

D'Orazio M. (1995) Trace element determination in igneous rocks by ICP-MS: results on ten international reference samples. *Periodico di Mineralogia* **64**, 315-328.

D'Orazio M., Folco L., Zeoli A. and Cordier C. (2011) Gebel Kamil: The iron meteorite that formed the Kamil crater (Egypt). *Meteorit. Planet. Sci.* **46**, 1179–1196.

Earth Impact Database. http://www.passc.net/EarthImpactDatabase/index.html. Accessed January 4, 2016.

Ebert M., Hecht L., Deutsch A. and Kenkmann T. (2013). Chemical modification of projectile residues and target material in a MEMIN cratering experiment. *Meteorit. Planet. Sci.* **48**, 134–149.

Field Code Changed

Ebert M., Hecht L., Deutsch A., Kenkmann T., Wirth R. and Berndt J. (2014) Geochemical processes between steel projectiles and silica-rich targets in hypervelocity impact experiments. *Geochim. Cosmochim. Acta* **133**, 257–279.

Fazio A., Folco L., D'Orazio M., Frezzotti M. L. and Cordier C. (2014) Shock metamorphism and impact melting in small impact craters on Earth: Evidence from Kamil Crater, Egypt. *Meteorit. Planet. Sci.* **49**, 2175-2200.

Folco L., Di Martino M., El Barkooky A., D'Orazio M., Lethy A., Urbini S., Nicolosi I., Hafez M., Cordier C., van Ginneken M., Zeoli A., Radwan A. M., El Khrepy S., El Gabry M., Gomaa M., Barakat A. A., Serra R. and El Sharkawi M. (2010) The Kamil Crater in Egypt. *Science* **329**, 804.

Folco L., Di Martino M., El Barkooky A., D'Orazio M., Lethy A., Urbini S., Nicolosi I., Hafez M., Cordier C., van Ginneken M., Zeoli A., Radwan A. M., El Khrepy S., El Gabry M., Gomaa M., Barakat A. A., Serra R. and El Sharkawi M. (2011) Kamil Crater (Egypt): Ground truth for small-scale meteorite impacts on Earth. *Geology* **39**, 179–182.

Folco L., D'Orazio M., Fazio A., Cordier C., Zeoli A., van Ginneken M., and El-Barkooky A. (2015) Microscopic impactor debris in the soil around Kamil Crater (Egypt): inventory, distribution, total mass and implications for the impact scenario. *Meteorit. Planet. Sci.* (accepted on 11.12.2014).

Gemelli M., D'Orazio M., and Folco L. (2015) Chemical analyses of iron meteorites using a hand-held X-ray fluorescence spectrometer. *Geostand. Geoanal. Res.* **39**, 55-69.

Gibbons R. V., Hörz F., Thompson T. D. and Brownlee D. E. (1976) Metal blebs in Wabar, Monturaqui and Henbury impactites. Proceedings, 7th Lunar Science Conference. *Geochim. Cosmochim. Acta Suppl.* **7**, 863–880.

Goderis S., Wittmann A., Zaiss J., Elburg M., Ravizza G., Vanhaecke F., Deutsch A., and P. Claeys (2013) Testing the ureilite projectile hypothesis for the El'gygytgyn impact: Determination of siderophile element abundances and Os isotope ratios in ICDP drill core samples and melt rocks. *Meteorit. Planet. Sci.* **48**, 1296-1324.

Grieve R. A. F. and Plant A. G. (1973) Partial melting on the lunar surface as observed in glass coated Apollo 16 samples. Proceedings, *4th Lunar Science Conference. Geochim. Cosmochim. Acta Suppl.* **4**, 667–679.

Güldemeister N., Wünneman K., Durr N., and Hiermaier S. (2013). Propagation of impact-induced shock waves in porous sandstone using mesoscale modeling. *Meteorit. Planet. Sci.* **48**, 115–133.

Field Code Changed

Hamann C., Hecht L., Ebert M. and Wirth R. (2013) Chemical projectile–target interaction and liquid immiscibility in impact glass from the Wabar craters, Saudi Arabia. *Geochim. Cosmochim. Acta* **121**, 291–310.

Hörz F., See T. H., Murali A. V. and Blanchard D. P. (1989) Heterogeneous dissemination of projectile materials in the impact melts from Wabar Crater, Saudi Arabia. In *Proc. 19th Lun. Planet. Sci. Conf.* pp. 697–709.

Hörz F., Mittlefehldt D. W., See T. H. and Galindo C. (2002). Petrographic studies of the impact melts from Meteor Crater, Arizona, USA. *Meteorit. Planet. Sci.* **37**, 501-531.

Langenhorst F. and Deutsch A. (2012). Shock metamorphism of minerals. *Elements* **8**, 31-36.

Kearsley A., Graham G., McDonnell T., Bland P., Hough R. and Helps P. (2004) Early fracturing and impact residue emplacement: Can modeling help to predict their location in major craters? *Meteorit. Planet. Sci.* ***39***, 247–265.

Kenkmann T., Deutsch A., Thoma K. and Poelchau M. H. (2013a) The MEMIN research unit: Experimental impact cratering. *Meteorit. Planet. Sci.* **48**, 1–2.

Kenkmann T., Trullenque G., Deutsch A., Hetcht L., Ebert M., Salge T., Schäfer F., and Thoma K. (2013b) Deformation and melting of steel projectiles in hypervelocity cratering experiments. *Meteorit. Planet. Sci.* **48**, 150–164.

Koeberl C., Claeys P., Hecht L. and McDonald I. (2012) Geochemistry of impactites. *Elements* **8**, 37–42.

Kowitz A., Güldemeister N., Reimold W. U., Schmitt R. T., and Wünnemann K. (2013) Diaplectic quartz glass and SiO_2 melt experimentally generated at only 5 GPa shock pressure in porous sandstone: Laboratory observations and meso-scale numerical modeling. *Earth Planet. Sci. Lett.* **384**, 17–26.

Kuper R., and Kröpelin, S. (2006) Climate-controlled Holocene occupation in the Sahara: Motor of Africa's evolution. *Science*, **313**, 803–807.

Melosh H. J. (2013) The contact and compression stage of impact cratering. In *Impact Cratering* (eds. G. R. Osinski and E. Pierazzo). Wiley-Blackwell, Chichester, West Sussex, U. K., pp. 32–42.

Mittlefehldt D. W., See T. H. and Hörz F. (1992) Dissemination and fractionation of projectile materials in the impact melts from Wabar Crater, Saudi Arabia. *Meteoritics* **27**, 361–370.

Nininger H. H. (1954) Impactite slag at Barringer Crater. *Am. J. Sci.* **252**, 277–290.

Osinski G. R. and Pierazzo E. (2013) Impact cratering: processes and products. In *Impact Cratering* (eds. G. R. Osinski and E. Pierazzo). Wiley-Blackwell, Chichester, West Sussex, U. K., pp. 125–145.

Field Code Changed

Osinski G. R., Grieve R. A. F., Marion C. and Chanou A. (2013) Impact melting. In *Impact Cratering* (eds. G. R. Osinski and E. Pierazzo). Wiley-Blackwell, Chichester, West Sussex, U. K., pp. 125–145.

Ott U., Merchel S., Herrmann S., Pavetich S., Rugel G., Faestermann T., Fimiani L., Gomez-Guzman J. M., Hain K., Korschinek G., Ludwig P., D'Orazio M. and Folco L. (2014) Cosmic ray exposure and pre-atmospheric size of the Gebel Kamil iron meteorite. *Meteorit. Planet. Sci*. **49**, 1365–1374.

Petzold A., and Hinz W. (1976) *Silikatchemie: Einführung in die Grundlagen.* Deutscher Verlag für Grundstoffindustrie, Leipzig, 219 pp..

Righter K., Drake M. J., Yaxley G. 1997. Prediction of siderophile element metal–silicate partition coefficients to 20 GPa and 2800 °C: the effects of pressure, temperature, oxygen fugacity, and silicate and metallic melt composition. *Phys. Earth Planet. Inter*. **100** 115–134.

Sighinolfi G. P., Sibilia E., Contini G. and Martini M. (2015) Thermoluminescence dating of the Kamil impact crater. *Meteorit. Planet. Sci.* **50**, 204-213.

Stöffler D. and Grieve R. A. F. (2007) Impactites, Chapter 2.11. In *Metamorphic Rocks: a Classification and Glossary of Terms, Recommendations of the International Union of Geological Sciences* (eds. D. Fettes and J. Desmons). Cambridge University Press, Cambridge, pp. 82–91, 111–125, and 126–242.

Stöffler D. and Langenhorst F. (1994) Shock metamorphism of quartz in nature and experiment: I. Basic observation and theory. *Meteoritics* **29**, 155–181.

Tamponi M., Bertoli F., Innocenti F. and Leoni L. (2003) X-ray fluorescence analysis of major elements in silicate rocks using fused glass discs. *Atti della Societá Toscana di Scienze Naturali, Memorie Serie A* **CVII**:73–80.

Urbini S., Nicolosi I., Zeoli A., El Khrepy S., Lethy A., Hafez M., El Gabry M., El Barkooky A., Barakat A., Gomaa M., Randwan A. M., El Sharkawi M., D'Orazio M. and Folco L. (2012) Geological and geophysical investigation of Kamil Crater, Egypt. *Meteorit. Planet. Sci.* **47**, 1842–1868.

Wittmann A., Kenkmann T., Schmitt R. T. and Stöffler D. (2006) Shock-metamorphosed zircon in terrestrial impact craters. *Meteorit. Planet. Sci.* **41**, 433–454.

Wünnemann K., Collins G. S., and Osinski G. R. 2008. Numerical modelling of impact melt production in porous rocks. *Earth Planet. Sci. Lett.* **269**:530-539

Figure Captions

Field Code Changed

Figure 1. Kamil crater, southwestern Egypt, and location map of the collected impact melt bombs studied in this work. Base map: enhanced true color QuickBird satellite image (22 October 2005; courtesy of Telespazio S.p.A.).

Figure 2. The Kamil crater target sandstones belonging to the Gilf Kebir Formation (Cretaceous). a) A panoramic view of the 45-m-diameter crater from the east. In the foreground, a ouadi cut shows the first ~1 m of the undisturbed stratigraphic sequence of the target in the proximity of the crater: pale sandstones (PS) with subhorizontal bedding; ejecta (Ej) and locally aeolian sand overlay pale sandstones. b) A detailed view of the ouadi cut. c) A detailed view of the local aeolian sand cover. d) The stratigraphic sequence of the target as seen on the northern upturned crater rim of the crater: (Ej) ejecta; (PS) the top of the sequence consists of a ~1.3 m thick pale sandstone bed of quartzarenite intercalated with wacke and siltstone levels; (PS') the uppermost pale sandstone level showing pervasive fracturing due to weathering; (RBS) reddish brown sandstones, consisting of very coarse- to coarse-grained, gritty and ferruginous quartzarenite, dominate the underlying sequence down to the crater bottom.

Figure 3. Impact glasses. a) Cut surface of an impact melt bomb of white vesicular glass (sample L04). b) Cut surface of an impact melt bomb of white glass coated by dark glass (sample L03). c) Cut surface of an impact melt bomb of dark glass (sample L06). The dark glass contains abundant fragments of shocked sandstone, pockets of lechatelierite, and rare fragments of meteorite. d) Dark glass (arrowed) stuck onto a meteorite shrapnel fragment. The side length of the scale cube is 1 cm. Abbreviations: MF = meteorite fragment; SC = shocked sandstone clasts; L = lechatelierite.

Figure 4. Photomicrographs of white glass impact melt lapilli and bombs. a) Detail of sample L03 coated by dark glass (optical microscope planar polarized light, PPL). b) Backscattered electron (BSE)-SEM image of the white impact melt bomb L04. The white glass is chemically homogeneous lechatelierite. Abbreviation: V = vesicle.

Figure 5. BSE-FESEM images of shocked quartzarenite clasts in white glass. Their constituting quartz grains consist of variable proportions of amorphous silica and crystalline domains (sample L09). a) A crystalline domain showing multiple sets (four) of planar to subplanar bands of amorphous silica material interpreted in this work as “melted relict PDF”. b) A detail of a partially crystalline quartz domain showing planar to subplanar amorphous silica bands and bearing a µm-sized bright inclusions (arrowed) of a yet to be determined phase. Note the radial pattern of fractures propagating into the host. c) The sharp contact between crystalline domain of shocked

Field Code Changed

quartz and lechatelierite. At the contact, lechatelierite is decorated by small elongated vesicles/cracks arranged geometrically, following the orientation of the PDF sets in the adjacent quartz grain. d) The gradual contact between diaplectic quartz and vesicular lechatelierite. Vesicle size increases away from the contact indicating coalescence. Abbreviations: Qtz = quartz; CD = crystalline domain; ASB = planar to subplanar amorphous silica bands ; D: diaplectic quartz; L = lechatelierite; V = vesicle.

Figure 6. Rare decomposed mineral grains and Fe-rich melts in white glass. a) BSE-SEM image of a partially decomposed zircon embedded in lechatelierite in sample M23. b) BSE-FESEM image of networks of veinlets and pockets of Fe-rich, Ni-free or Fe-Ca-Mg-rich Ni-free silicate melts occasionally occur around vesicle in lechatelierite. c) The end of a Fe-rich, Ni-free melt veinlet in lechatelierite showing immiscibility textures. Note the fractal distribution of micro-to-nano-blebs at the end of the veinlet.

Figure 7. Photomicrograph (a) and FEG-SEM (b-g) images of dark glass impact melt bomb (sample L6). a) PPL image showing the main optical features of the dark glass: old-yellow to opaque glass containing clasts of shocked sandstone, lechatelierite, and diaplectic glass. b) BSE image of the same area; note the occurrence of Ni-Fe metal blebs embedded in the dark glass. c) BSE image of the shocked sandstone clasts showing PDF (inset) and multiple sets of planar to Subplanar bands of amorphous silica material (interpreted in this work as "melted relict PDF") and surrounded by a SiO_2-rich melt and pockets and veinlets of dark glass. d) BSE image of a Ni-Fe metal bleb in lechatelierite. The bleb consists mainly of cellular grains of Ni-Fe metal with minor intergranular S- and P-rich materials. e) BSE image of the complex contact between dark glass and a quartz grain of a shocked sandstone clast. The quartz grain is surrounded by lechatelierite. Lechatelierite and adjacent dark glass show an interfingered contact indicating coexistence of the silica and dark glass melts and their immiscibility. Few µm away from the contact, the dark glass shows fine immiscibility textures. f) BSE image of an example of immiscibility texture due to the solidification of two immiscible melts: silica and dark glasses. g) BSE image of an opaque dark glass border. Opaque dark glass is decorated by crystallite of Fe-oxides. At the edge of the sample a few µm-thick Ni-rich melt occurs. Abbreviations: DG = Dark glass; OPDG = opaque dark glass; D = diaplectic quartz glass; L = lechatelierite; V = vesicle; Ni-Fe M = Ni-Fe metal blebs; SC = shocked sandstone; IM = intergranular melt; S = S-rich material; P = P-rich material.

Field Code Changed

Figure 8. Iron (wt%) vs. Ni (wt%) semilogarithmic abundance diagram, showing the composition of the Ni-Fe metal blebs (42 point analyses from several blebs) occurring in the dark glass (sample L06) in relationship with the bulk composition of the Gebel Kamil iron meteorite. In addition, compositional data of H-Ni and VH-Ni metal blebs (28 and 4 point analyses from 9 and 2 samples, respectively) occurring in the dark glass of the microscopic impact melt beads studied by Folco et al., (2015) are reported.

Figure 9. Iron (wt%) vs. Si (wt%) logarithmic abundance diagrams for (a) lechatelierite and dark glass (samples L06 and L03) and of (b) lechatelierite and dark glass of the microparticles studied by Folco et al., (2015). The chemical composition of the Gebel Kamil iron meteorite, kaolinitic matrix, and the dark glass experimentally produced by MEMIN experiment (Ebert et al., 2013) are reported for comparison in both diagrams. The dashed line is the mixing line between Gebel Kamil and pure SiO_2.

Figure 10. Iron (wt%) vs. Ni (µg g^{-1}) and Co (µg g^{-1}) vs. Ni (µg g^{-1}) vs Co (µg g^{-1}) showing the composition variations of target rocks and impact melt lapilli and bombs from Kamil Crater. Dashed lines represent the Ni/Fe and Ni/Co ratios of the Gebel Kamil iron meteorite.

Figure 11. Sequence of four BSE-FESEM images showing the progressive enlargement of PDFs till the almost complete melting of the quartz (amorphous SiO_2 material is darker than quartz because its density is lower). a) PDFs in shocked sandstone (sample L23; Fazio et al. 2014). b) Multiple sets of planar to subplanar bands of amorphous silica material with micrometric spacing, abutting silica glass pockets in shocked sandstone (sample L23; Fazio et al. 2014). c) Multiple sets of subplanar bands of amorphous silica material with greater thickness than in Fig. 11b occurring in a former quartz grain embedded in a white glass bomb (sample L09; this work). d) Thick subplanar bands of amorphous silica material occurring in a former quartz grain embedded a white glass bomb (sample L09; this work). The amorphous material dominates the original crystal volume. Here the former crystalline quartz has almost completely transformed in silica glass, namely lechatelierite.

Figure 12. Sketch of the impact melting process at Kamil Crater. a) At the end of the contact and compression stage the shock wave passes thought the target and the projectile. The target is highly compressed and the projectile is heated and highly deformed. Shock pressure rapidly decrease from 50 GPa at the contact point up to <5 GPa at the crater wall (isobars are indicated by dashed gray curved lines). b) Close-up view of the black rectangular area in (a) showing the formation of a projectile and a target liquid. The projectile and the target liquid chemically and physically interact at the contact zone. c) Detailed view of the interaction zone outlined by a black rectangle in (b) at

Field Code Changed

Kamil Crater. The geochemical interaction between the projectile melt and a target silicate melt under oxidizing conditions generated a mixed melt which eventually gave rise to the dark glass. Another immiscible target melt, consisting of highly polymerized pure SiO_2 melt did not geochemically interact with the projectile and eventually gave rise to the white glass. The two target melts are the reflection of the cm-scale intercalations of quartzarenite and wacke/siltstones levels. Immiscibility was favored by the rapid shock heating and quenching expected in small impact craters such as Kamil Crater.

Field Code Changed

Table 1

Table 1. Bulk chemical composition of target rocks at Kamil Crater. Major (oxide wt%) and trace elements (µg g^{-1}) were determined by XRF and ICP-MS analyses. The major element composition of the kaolinite-rich matrix occurring in both pale and reddish brown sandstones was determined by EPMA. Modified after Folco et al. (2015).

	Pale sandstones			Reddish brown sandstones
	Quartzarenite, negligible matrix contents	Wacke with siltstone levels	Kaolinite-rich matrix	Quartzarenite, ~ 5 vol.% matrix
Sample	M26	L13	L13 - L14[a]	M27
Major elements				
SiO_2	99.8	87.8	44.5	95.7
TiO_2	0.07	1.15	0.55	0.09
Al_2O_3	0.25	10.1	34.8	1.98
FeO_T	0.10	0.66	1.18	1.54
MnO	<0.01	<0.01	<0.01	0.06
MgO	0.18	0.14	0.06	0.25
CaO	0.05	0.11	0.04	0.31
Na_2O	0.05	0.13	0.04	0.08
K_2O	<0.01	0.04	0.05	<0.01
P_2O_5	<0.~~01~~02	0.06	0.09	0.04
sum	100.5	100.2	81.3[b]	100.1
L.O.I.	0.65	3.91		1.19
Trace elements				
V	3.0	53		32
Cr	20	57		9.5
Ni	6.9	7.3		13
Co	0.5	2.1		10
Cu	5.2	8.9		15
Ni/Fe	0.009	0.001		0.001
Ni/Co	13.2	3.51		1.19

[a] Average of eighteen EPMA analyses from samples L13 and L14.
[b] The low total of the average of the EPM analyses of kaolinite is assumed to be due to the water content of this mineral (~19 wt%).
FeO_T: total iron as FeO.
Abbreviations: L.O.I., Loss On Ignition.

Table 2

Table 2. Location and description of impact melt lapilli and bombs from Kamil Crater studied in this work (Table modified after Fazio et al., 2014).

Sample	Latitude N	Longitude E	Location	Description
L15	22°01'6.05"	26°05'15.77"	Inside the crater	Lapillus made of dark glass with inclusions of sandstone clasts, diaplectic quartz glass and lechatelierite. Metallic blebs are scattered in the dark glass.
M23	22°01'5.69"	26°05'16.27"	Inside the crater	Bomb made of white lechatelierite. Vesicles are rounded and generally millimetric.
L08	22°01'4.05"	26°05'16.53"	52 m due SSE of CR	Bomb made of white lechatelierite partially coated by < 2 mm thick dark glass envelope.
L09	22°01'4.01"	26°05'16.57"	52 m due SSE of CR	Lapillus made of white lechatelierite locally stained by reddish-brown material (iron-oxi-hydroxides). Relicts of highly shocked quartz grains (melted PDFs, diaplectic quartz glass) are common in this sample.
L05	22°01'5.29"	26°05'18.17"	57 m due E of CR	Lapillus made of dark glass with inclusions of sandstone clasts, diaplectic quartz glass and lechatelierite. Metallic blebs are scattered in the dark glass.
L06	22°01'5.27"	26°05'18.14"	57 m due E of CR	Bomb made of dark glass with inclusions of sandstone clasts, diaplectic quartz glass and lechatelierite. Metallic blebs are scattered in the dark glass. Rare occurrence of fragments of the iron projectile Gebel Kamil.
$E30_{m.s.}$	22°01'3.39"	26°05'16.44"	57 m due ESE of CR	Dark glass found stuck to the surface of a shrapnel of the iron meteorite Gebel Kamil. Inclusions of sandstone clasts, diaplectic quartz glass and lechatelierite are common. Metallic blebs are scattered in the dark glass.
$MNA07_{m.s.}$	22°01'4.51"	26°05'18.11"	61 m due SSE of CR	Dark glass found stuck to the surface of a shrapnel of the iron meteorite Gebel Kamil. Inclusions of sandstone clasts, diaplectic quartz glass and lechatelierite are common. Metallic blebs are scattered in the dark glass.
L03	22°01'7.91"	26°05'19.88"	120 m due ENE of CR	Bomb made of white lechatelierite completely coated by < 2 mm thick dark glass envelope.
L04	22°01'7.93"	26°05'19.92"	120 m due ENE of CR	Bomb made of white lechatelierite. Vesicles are elongated and can be up to 3 mm in size.

Abbreviations: CR: crater rim; m.s.: meteorite shrapnel.

Table 3

Table 3. Representative bulk chemical compositions of impact melt lapilli and bombs from Kamil Crater. Major elements (wt%) were determined by XRF. Trace elements (µg g^{-1}) were determined by ICP-MS.

	White glass	White glass	White glass coated by dark glass	White glass coated by dark glass	Dark glass
Sample	M23	L04	L03	L08	L06
SiO_2	99.9	99.4	96.2	98.7	74.2
TiO_2	0.08	0.06	0.15	0.05	0.57
Al_2O_3	0.46	0.69	1.76	0.64	5.80
FeO_T	0.40	0.42	0.77	0.84	14.6
MnO	0.02	0.02	0.03	0.02	0.18
MgO	0.22	0.43	0.30	0.31	0.22
CaO	0.12	0.65	0.34	0.34	0.37
Na_2O	0.10	0.11	0.09	0.10	0.07
K_2O	<0.01	0.04	0.04	0.02	0.06
P_2O_5	<0.01	0.02	0.03	0.02	0.22
sum	101.3	101.8	99.7	101.0	96.3
L.O.I.	0.53	1.89	0.99	1.21	-1.38
Trace elements					
V	11	11	16	20	227
Cr	24	43	18	21	357
Ni	34	18	121	233	22950
Co	1.8	1.2	7.2	11	908
Cu	12	24	15	21	87
Ni/Fe	0.011	0.005	0.020	0.035	0.203
Ni/Co	19.3	14.6	16.8	22.1	25.3

FeO_T: total iron as FeO
Abbreviations: L.O.I.: Loss On Ignition.

Table 4

Table 4. Representative electron microprobe analyses (oxide wt%) of white glass of impact melt lapilli and bombs.

	SiO_2	TiO_2	Al_2O_3	FeO_T	MnO	NiO	MgO	CaO	Na_2O	K_2O	P_2O_5	Sum
White glass/Lechatelierite (samples L03 and L04)												
Avg. (n=8)	98.3	0.02	0.14	0.07	0.02	<0.02	0.02	0.02	0.05	0.02	0.02	98.6
±1σ	1.44	b.d.l.	0.15	0.08				0.01	0.01	0.01		
Diaplectic quartz grains (sample L09)												
Avg. (n=8)	98.6	<0.01	0.15	0.11	0.02	<0.02	<0.01	<0.01	0.03	0.03	0.02	98.9
±1σ	0.50		0.14	0.08					0.01	0.01	0.00	
Fe-rich silicate melt (sample L04)												
Avg. (n=6)	21.3	0.04	0.54	65.3	0.70	<0.02	2.62	2.46	0.05	<0.01	0.23	93.2
±1σ	9.35	0.02	0.23	7.82	0.48		2.02	1.94			0.11	

Abbreviations: avg.: average; b.d.l.: below detection limit; n: number of analyses.
Detection limits are 0.04 wt% for Na_2O, 0.02 wt% for Al_2O_3 and NiO, and 0.01 wt% for MgO, CaO, K_2O, FeO, MnO, TiO_2, and P_2O_5.
FeO_T: total iron as FeO.

Table 5

Table 5. Representative electron microprobe analyses (oxide wt%) of dark glass and shocked quartz clasts in impact melt lapilli and bombs of dark glass.

	SiO_2	TiO_2	Al_2O_3	FeO_T	MnO	NiO	MgO	CaO	Na_2O	K_2O	P_2O_5	Sum
Dark glass (sample L06)												
Avg. (n=102)	66.9	0.70	7.84	21.3	0.39	0.7	0.14	0.54	0.08	0.13	0.41	98.8
±1σ	22.2	0.49	5.33	15.0	0.28	1.5	0.09	0.43	0.03	0.09	1.91	
Dark glass (sample L03)												
Avg. (n=22)	79.0	0.46	8.50	9.8	0.21	<0.02	0.16	0.17	0.06	0.13	0.14	98.5
±1σ	12.1	0.20	5.24	6.8	0.18		0.11	0.14	0.02	0.10	0.08	
Shocked quartz clasts												
Avg. (n=5)	99.5	0.04	0.05	0.04	0.19	0.04	0.03	0.03	0.05	<0.01	<0.01	99.8
±1σ	0.88		0.01	0.01	0.15	0.03		0.01				
Silica melt pockets												
Avg. (n=25)	99.1	0.04	0.06	0.04	0.19	0.03	0.02	0.02	<0.04	0.02	<0.01	99.4
±1σ	0.47	0.02	0.07	0.02	0.14	0.01	0.01					

Abbreviations: avg., average; b.d.l., below detection limit; n, number of analyses.
Detection limits are 0.04 wt% for Na_2O, 0.02 wt% for Al_2O_3 and NiO, and 0.01 wt% for MgO, CaO, K_2O, FeO, MnO, TiO_2, and P_2O_5.
FeO_T: total iron as FeO.

Table 6

Table 6. Bulk composition of the Gebel Kamil iron meteorite (HH-XRF; Gemelli et al., 2015), representative electron microprobe analyses (oxide wt%) of Ni-Fe metal blebs within dark glass (this work; sample L06), ranging in diameter from 15 to 170 µm.

	Si	P	S	Fe	Co	Ni	Sum
Gebel Kamil	<0.05	0.04	0.02	78.5	0.69	20.6	99.8
Ni-Fe metal blebs (Avg.; n=42)	0.11	0.62	0.31	34.1	1.84	63.5	100.2
±1 σ	0.05	0.74	0.86	3.73	0.14	4.01	

Abbreviations: avg., average; n, number of analyses.

Figure 1

Click here to download high resolution image

Figure 2

Click here to download high resolution image

Figure 3

Click here to download high resolution image

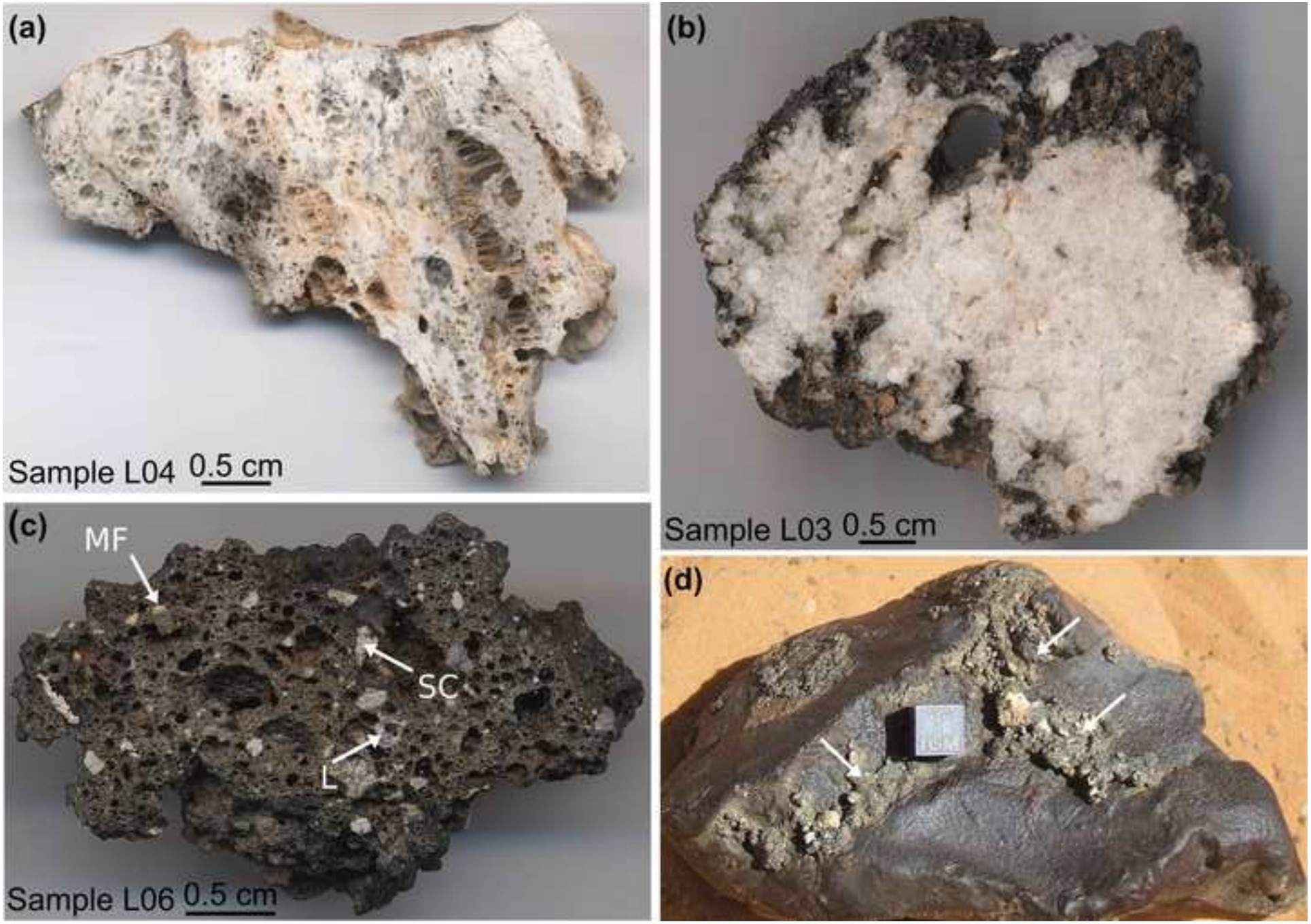

Figure 4

Click here to download high resolution image

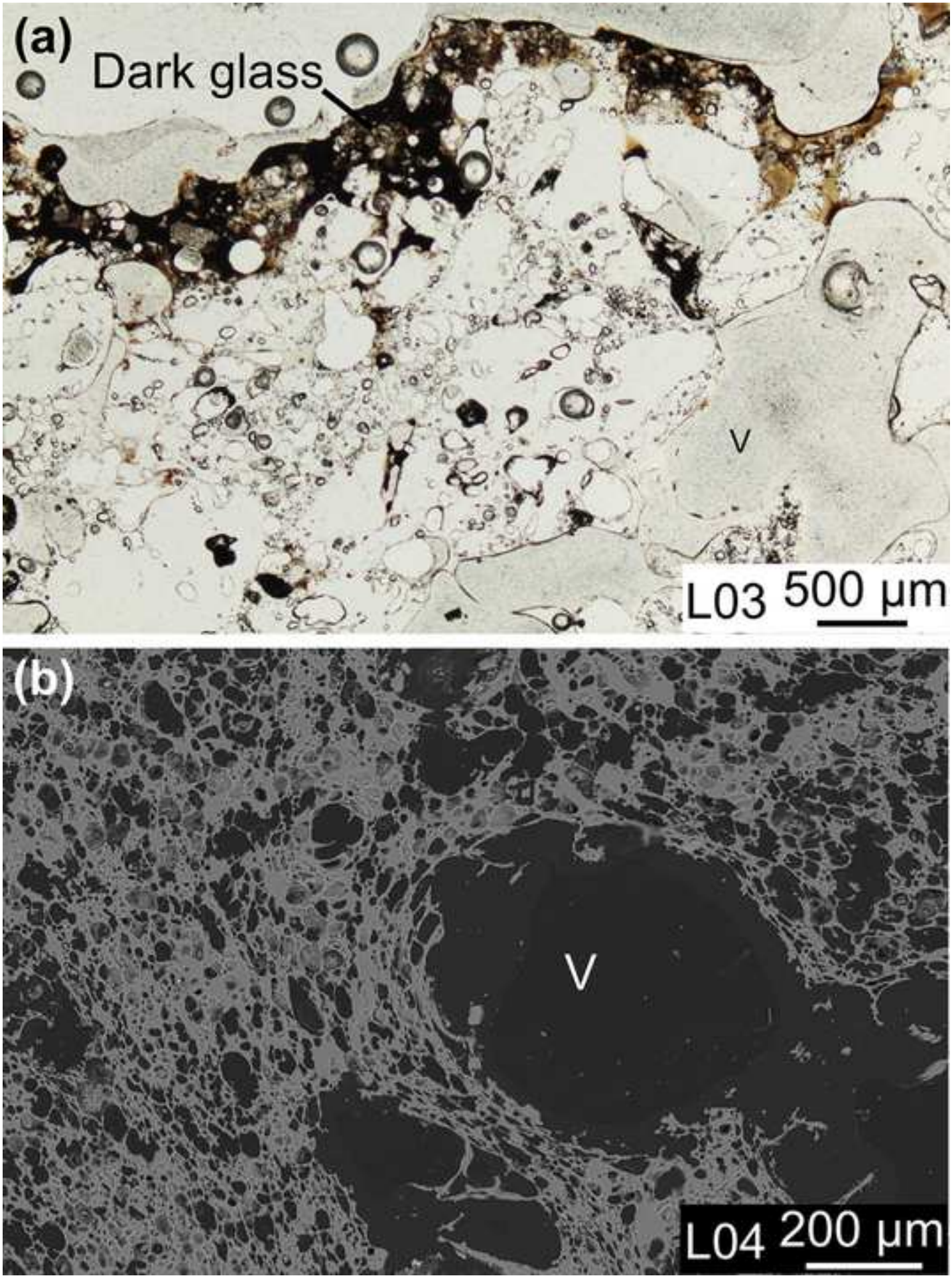

Figure 5

Click here to download high resolution image

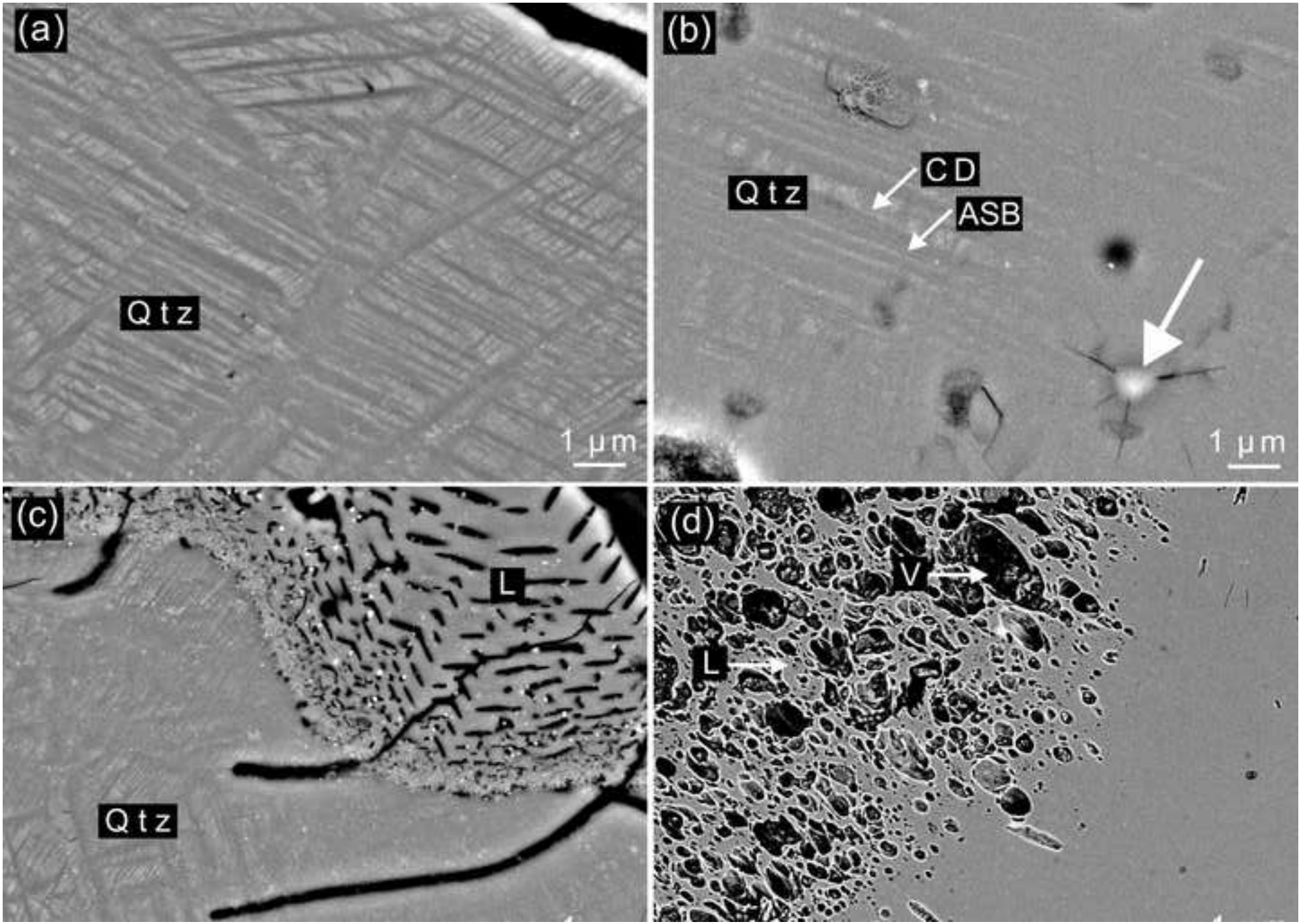

Figure 6

Click here to download high resolution image

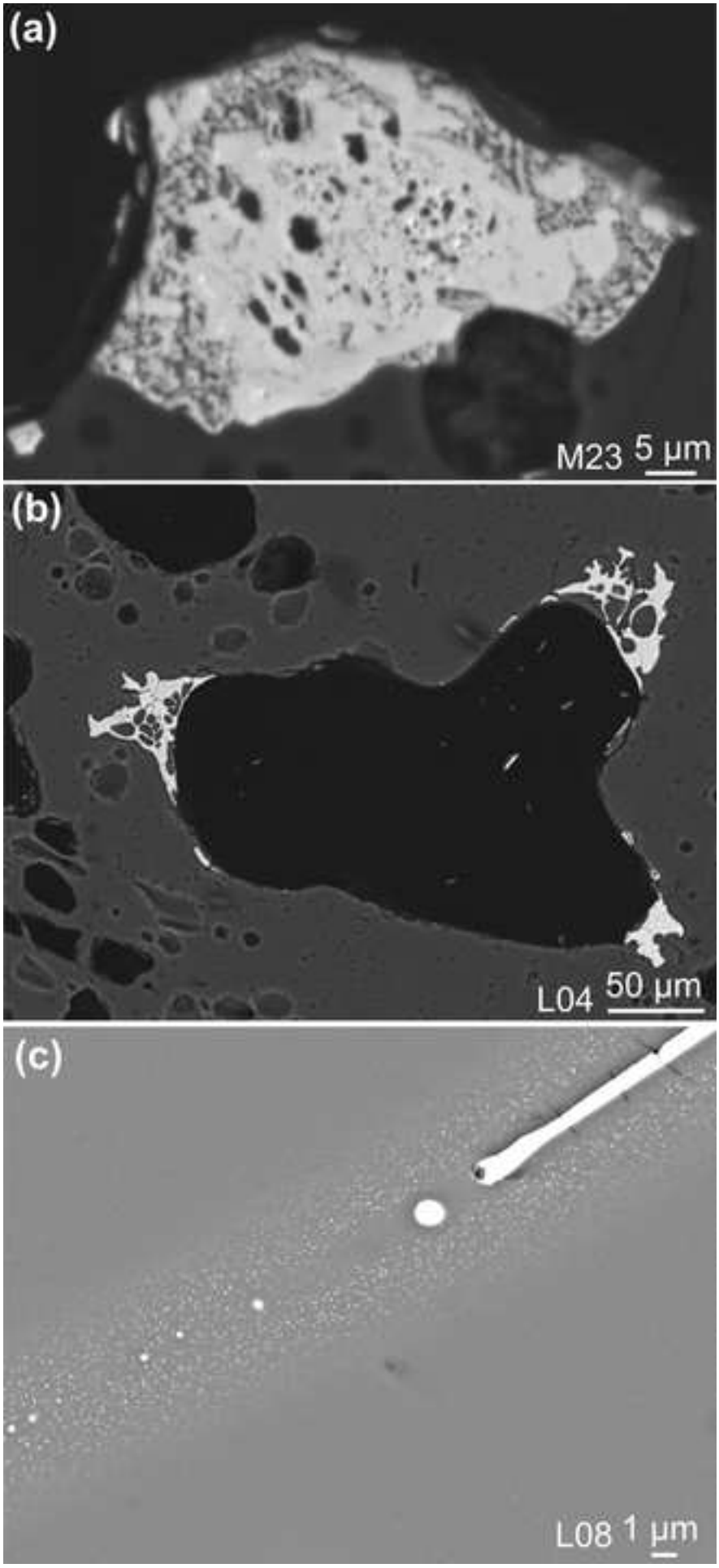

Figure 7

Click here to download high resolution image

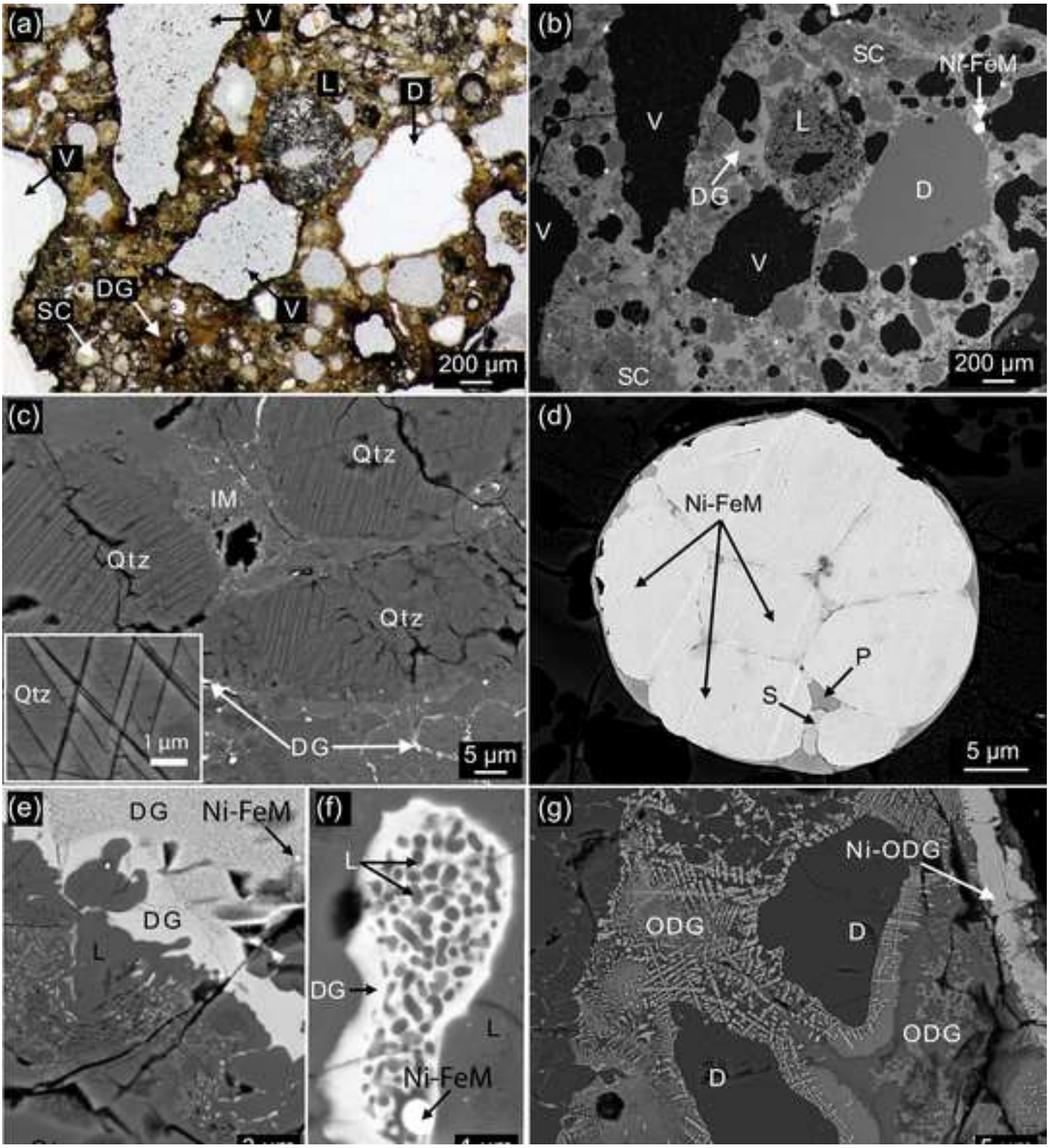

Figure 8

Click here to download high resolution image

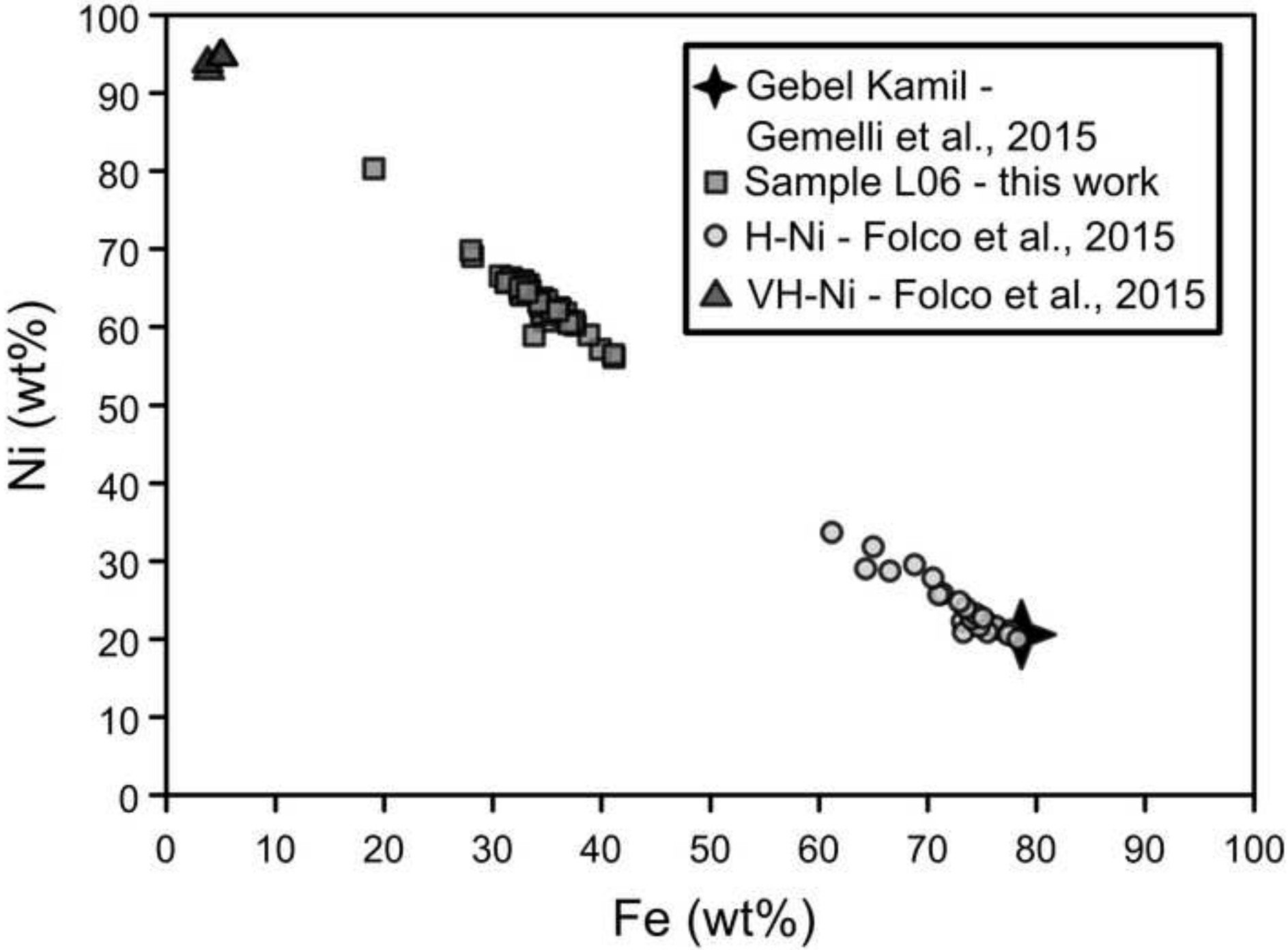

Figure 9

Click here to download high resolution image

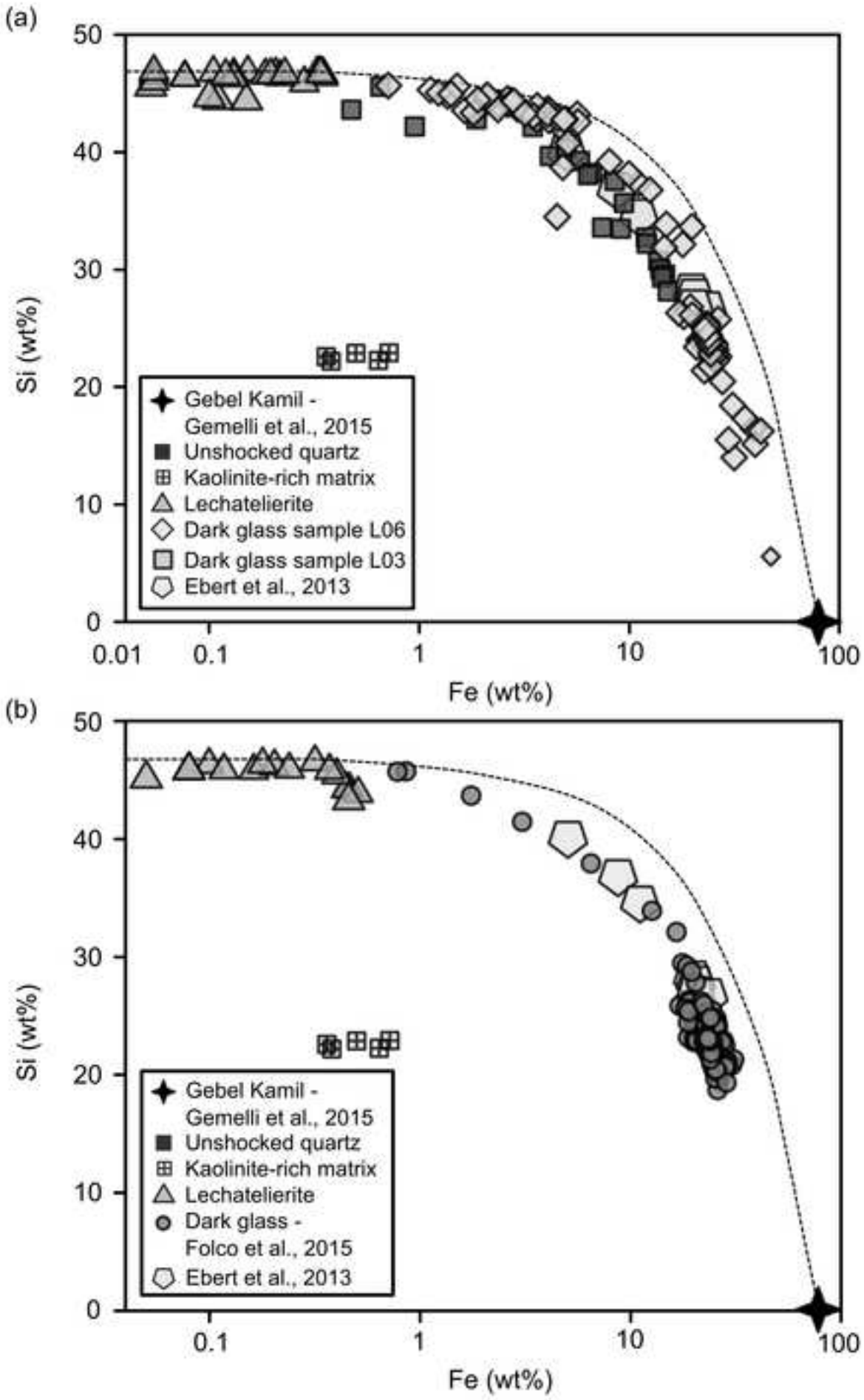

Figure 10
Click here to download high resolution image

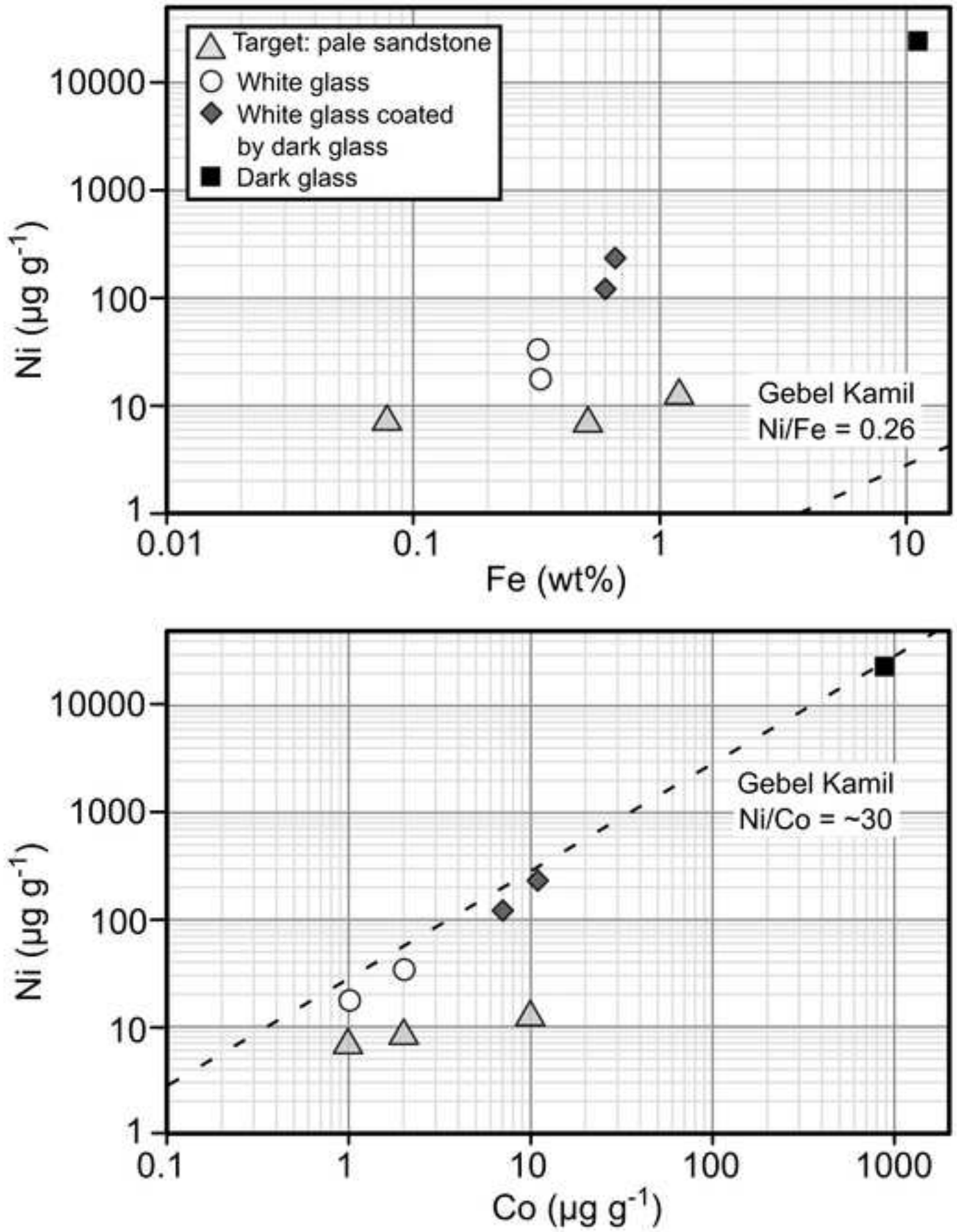

Figure 11

Click here to download high resolution image

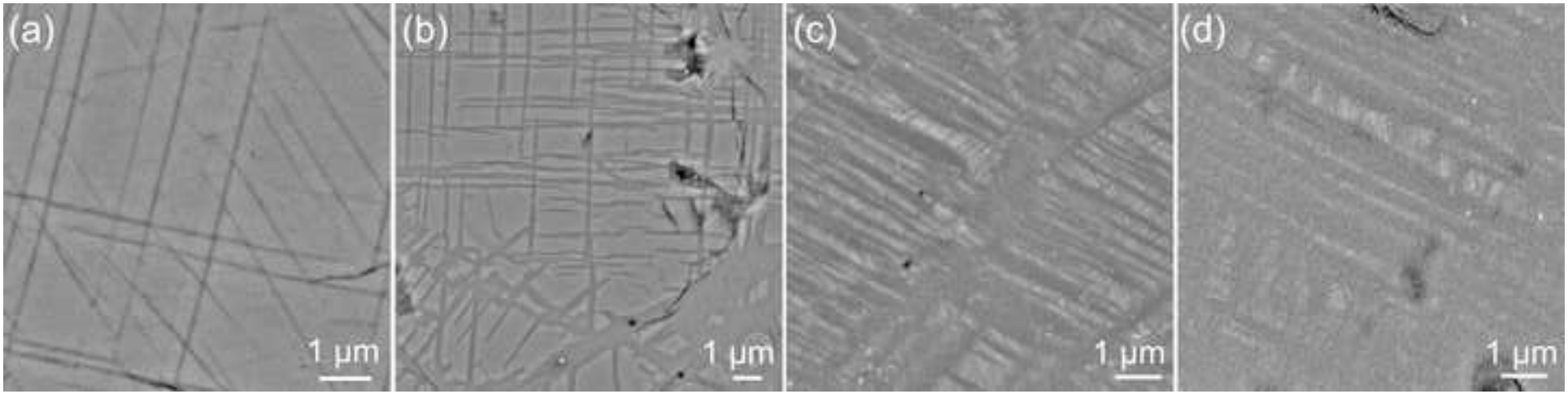

Figure 12

Click here to download high resolution image